Colloquium: Positronium physics and biomedical applications

Steven D. Bass [*]

*Kitzbühel Centre for Physics, 6370 Kitzbühel, Austria
and Marian Smoluchowski Institute of Physics, Jagiellonian University,
PL 30-348 Krakow, Poland*

Sebastiano Mariazzi [†]

*Department of Physics, University of Trento, via Sommarive 14, 38123 Povo, Trento, Italy
and TIFPA/INFN, via Sommarive 14, 38123 Povo, Trento, Italy*

Pawel Moskal [‡] and Ewa Stępień [§]

*Marian Smoluchowski Institute of Physics, Jagiellonian University, PL 30-348 Krakow, Poland
and Center for Theranostics, Jagiellonian University, 31-034 Krakow, Poland*

(published 10 May 2023)

Positronium is the simplest bound state, built of an electron and a positron. Studies of positronium in vacuum and its decays in medium tell us about quantum electrodynamics (QED) and about the structure of matter and biological processes of living organisms at the nanoscale, respectively. Spectroscopic measurements constrain our understanding of QED bound state theory. Searches for rare decays and measurements of the effect of gravitation on positronium are used to look for new physics phenomena. In biological materials positronium decays are sensitive to the intermolecular and intramolecular structure and to the metabolism of living organisms ranging from single cells to human beings. This leads to new ideas of positronium imaging in medicine using the fact that during positron emission tomography (PET) as much as 40% of positron annihilation occurs through the production of positronium atoms inside the patient's body. A new generation of the high sensitivity and multiphoton total-body PET systems opens perspectives for clinical applications of positronium as a biomarker of tissue pathology and the degree of tissue oxidation.

CONTENTS

[*]Steven.Bass@cern.ch
[†]Sebastiano.Mariazzi@unitn.it
[‡]P.Moskal@uj.edu.pl
[§]E.Stepien@uj.edu.pl

I. INTRODUCTION

Positronium "atoms" are special as short-lived bound states of an electron e^- and its antiparticle, the positron e^+. They are at the same time their own "antiatoms." Positronium is topical in both fundamental physics research and applications in biology and medicine, with the prime focus here on its role in new positron emission tomography (PET) technologies.

The physics of positronium is expected to be described by quantum electrodynamics (QED), which is our most accurately tested theory, up to 1 part in 10^{12}, with small radiative corrections from the strong and weak interactions. Recent experiments have revealed some surprises pushing the boundaries of QED bound state theory (Adkins, Cassidy, and Pérez-Ríos, 2022) with the observation of anomalies up to 4.5 standard deviations at the precision of 10^{-4} between

measurements and theory in hyperfine splittings of positronium energy levels. Possible couplings of positronium to new interactions are being probed through precision symmetry tests and rare decay measurements. These experiments promise to yield a new understanding of charged lepton bound states.

While there are uncertainties at this level, positronium is sufficiently well understood to enable its role in applications from fundamental physics experiments involving the study of gravitation on antimatter to diagnostic tests in medicine. About 40% of the positrons in PET scans go through positronium formation and decay in the body. Building on this result, positronium is being explored as a vital ingredient in next generation total-body PET devices where two or more photons are detected simultaneously from individual positronium decays using the new technique of multiphoton tomography. Quantum entanglement of the emitted photons may further enhance the diagnostic power.

In this Colloquium we explore this physics first with an introduction to positronium and then covering the present status of precision positronium measurements and current anomalies between data and bound state theory. We explain the mechanisms of positronium formation and decays in materials and then, with a key focus on biological substances, the application in next generation PET devices. New positronium imaging technologies have the promise of revolutionizing total-body PET imaging with the benefit of medical diagnostics.

Positronium comes in two ground states: $^1S_0$ parapositronium, denoted p-Ps, where the spins of the electron and positron add up to zero, and $^3S_1$ orthopositronium, denoted o-Ps, where the spins of the electron and positron add up to 1. The binding energy

$$E_B \approx -m_e \alpha^2/4 = -6.8 \text{ eV} \qquad (1)$$

is much less than the electron mass $m_e = 0.51$ MeV, with $\alpha \approx 1/137$ the fine structure constant. p-Ps is slightly lighter, by 0.84 meV, due to the interaction between the electron and positron spins and also the existence of virtual annihilation processes (Cassidy, 2018).

Spin-0 p-Ps decays in vacuum to two photons with a lifetime of 125 ps and spin-1 o-Ps decays to three photons with a lifetime of 142 ns. The factor of more than a 1000 times longer lifetime of o-Ps enables an efficient distinction between these two states. The main reason for the difference in lifetimes comes from an extra factor of the fine structure constant α that enters with the three-photon decay compared to two-photon decays.

Positronium was first discovered by Deutsch (1951) following the initial prediction of positron antimatter by Dirac (1931), the discovery of the positron by Anderson (1933), and prediction of the e^+e^- bound state by Mohorovicic (1934).

The two positronium ground states o-Ps and p-Ps, being bound states of e^- and e^+, are both odd under parity transformations P. Under charge conjugation C o-Ps is odd and p-Ps is even. C symmetry conservation determines the decays of o-Ps and p-Ps into an odd and even number of photons, respectively, with photons being C symmetry odd

(Berko and Pendleton, 1980; Cassidy, 2018). Since positronium is unstable with leading decay to two or three massless photons (for p-Ps and o-Ps), it is not an eigenstate of time reversal transformations T. This property has the consequence that final state interactions involving photon-photon rescattering interactions at higher order in α can mimic a small CP and CPT violation in positronium decays.

Positronium spectroscopy research is presently focused on precision measurements of hyperfine structure (HFS) and also Rydberg states, the latter with the aim of determining the Rydberg constant based on positronium (Cassidy, 2018). Several few standard deviation discrepancies have been reported between the precision HFS measurements and QED bound state calculations performed using the simplifications of nonrelativistic QED effective theory, with the differences entering at precision of a few parts in 10 000 or less (Karshenboim, 2004; Heiss *et al.*, 2018; Gurung *et al.*, 2020). Positronium decay measurements have thus far been in agreement with QED bound state theory at similar accuracy. An important ingredient in modeling is that positronium should satisfy the fundamental symmetries of its constituents. Rare decays are strongly constrained by precision measurements of the electron anomalous magnetic moment and electric dipole moment, with a prime topic being the search for invisible decays in connection with possible dark matter candidates called mirror matter particles (Vigo *et al.*, 2020). In connection with gravitation, positronium is also playing an important role in precision tests of gravity on antimatter planned at CERN: the experiments AEgIS (Doser *et al.*, 2018) and GBAR (Perez and Sacquin, 2012; Dufour *et al.*, 2015).

In materials, positronium formation and decay is sensitive to the immediate chemical environment. This has interesting medical applications with sensitivity to the healthiness of biological tissue where positronium is produced and may serve as a hallmark telling one about the size of intermolecular and intramolecular voids and the concentration in them of biomolecules such as oxygen (O_2) (Moskal, Jasinska *et al.*, 2019). These properties of positronium suggest its role as a biomarker, a characteristic that is objectively measured and evaluated as an indicator of normal biological (healthy) or pathogenic (cancerous) processes. This result has inspired new ideas for positronium imaging, a new technique in medical diagnosis that enables imaging of positronium properties inside the bodies of living organisms (Moskal *et al.*, 2021a). Electromagnetic decays of positronium should exhibit quantum entanglement of the final state photons (Acin, Latorre, and Pascual, 2001; Hiesmayr and Moskal, 2017), with ideas for how this may be exploited in positronium imaging and next generation PET devices discussed by McNamara *et al.* (2014) and Hiesmayr and Moskal (2019).

The plan of this Colloquium is as follows. In Sec. II we discuss the status of precision QED measurements and theory, which constrains detailed modeling of the positronium system. In Sec. III we turn our attention to materials systems where positronium production and decays depend on the chemical environment. This leads to discussions of positronium in fundamental physics experiments and medical applications. Positronium spectroscopy, its role in the AEgIS and GBAR antimatter experiments at CERN, and Bose-Einstein condensates as well as quantum entanglement in positronium

decays are summarized in Sec. IV. Biological and medical applications are discussed in Secs. V and VI, including new developments with positronium imaging and the emerging application of positronium as a biomarker for assessing the tissue pathology *in vivo*. Conclusions and an outlook on future opportunities are given in Sec. VII.

Complementary reviews of positronium physics, each with a different emphasis, were given by , Berko and Pendleton (1980), Gninenko, Krasnikov, and Rubbia (2002), Karshenboim (2004), Karshenboim (2005), Goworek (2014), Nagashima (2014), Cassidy (2018), Bass (2019), and Adkins, Cassidy, and Pérez-Ríos (2022). Introductions to applications in medicine and biology were given by Harpen (2004) and Moskal, Jasinska *et al.* (2019).

II. POSITRONIUM IN THE STANDARD MODEL

As a bound state of an electron and positron with dynamics determined by QED, the physics of positronium is strongly constrained by precision QED observables. QED is a gauge theory invariant under local $U(1)$ transformations of the phase of the electron and other charged fermions. The QED Lagrangian reads

$$\mathcal{L} = \bar{\psi} i \gamma^\mu (\partial_\mu + i e A_\mu) \psi - m_e \bar{\psi}\psi - \frac{1}{4} F_{\mu\nu} F^{\mu\nu}. \quad (2)$$

In Eq. (2) ψ represents the electron field, A_μ is the photon, e is the electric charge, and $F_{\mu\nu} = \partial_\mu A_\nu - \partial_\nu A_\mu$ is the electromagnetic field tensor; $\alpha = e^2/4\pi$ is the fine structure constant. Electrons and positrons interact through massless photon exchange.

Measurements of the electron's anomalous magnetic moment $a_e = (g-2)/2$ and atomic physics measurements of the fine structure constant using atom interferometry with cesium (Cs) and rubidium (Rb) atoms are consistent with each other and with QED theory to 1 part in 10^{12}.

The electron's anomalous magnetic moment a_e is nonvanishing, differing from the Born term level Dirac value $a_e = 0$ by a perturbative QED expansion in α that is known to $\mathcal{O}(\alpha^5)$ (Aoyama, Kinoshita, and Nio, 2018). Precision measurement of a_e thus allows determination of the fine structure constant. The atom interferometry measurements give a direct measurement of α. Any "beyond the standard model" effects involving new particles active in radiative corrections would give an extra correction to a_e but not the direct Cs and Rb interferometry measurements. Thus, comparing these different determinations of α gives a precision test of QED and constrains possible new physics scenarios.

QED radiative corrections involving heavy muons and tau leptons as well as hadronic corrections from quantum chromodynamics (QCD) each enter a_e at the level of 2×10^{-12} and weak interactions at the level of 3×10^{-14}, so the anomalous magnetic moment is a precise test of electron-photon interactions.

The most accurate measurement of a_e is (Hanneke, Fogwell, and Gabrielse, 2008)

$$a_e^{\text{exp}} = 0.001\,159\,652\,180\,73(28). \quad (3)$$

If one substitutes the most recent direct α measurements from atom interferometry measurements using both Cs (Parker *et al.*, 2018),

$$1/\alpha|_{\text{Cs}} = 137.035\,999\,046(27), \quad (4)$$

and Rb (Morel *et al.*, 2020),

$$1/\alpha|_{\text{Rb}} = 137.035\,999\,206(11), \quad (5)$$

into the perturbative QED expansion for a_e, one finds agreement to 1 part in 10^{12} when comparing with a_e^{exp} in Eq. (3), viz.,

$$a_e^{\text{exp}} - a_e^{\text{th}}|_{\text{Cs}} = (-88 \pm 36) \times 10^{-14} \quad (6)$$

and

$$a_e^{\text{exp}} - a_e^{\text{th}}|_{\text{Rb}} = (+44 \pm 30) \times 10^{-14}, \quad (7)$$

when we substitute the α values in Eqs. (4) and (5) into the QED perturbative expansion for a_e to obtain the value $a_e^{\text{th}}|_{\text{atom}}$.

QED is working well. For practical calculations of positronium spectroscopy and decays one needs an extra step of QED bound state theory.

Bound state calculations are difficult, even in QED. Some model simplifications are needed to make the calculations tractable. The nonrelativistic Schrödinger equation for the $e^- e^+$ system gives the correct leading order expression for the positronium binding energy [Eq. (1)]. With this in mind a rigorous effective theory formalism has been developed for calculating positronium spectroscopy and decays to multiple-photon final states. This is called nonrelativistic QED (NRQED) (Caswell and Lepage, 1986); for reviews see Kinoshita and Lepage (1990), Labelle (1992), and Karshenboim (2004).

NRQED involves a perturbation expansion in $v/c \sim \alpha$, where v is the electron and positron velocities in the positronium, c is the speed of light, and α is the fine structure constant. This approximation allows for possible calculations. One introduces a cutoff on relativistic effects from the fundamental QED Lagrangian [Eq. (2)]. These are then implemented through adding extra "correction terms" in the NRQED Lagrangian. The parameters are adjusted to fit the results of experiments, and the NRQED Lagrangian is then used to calculate new observables. One assumes that the incident electron-positron pair is nonrelativistic, with relativistic terms in the interactions taken care of by the NRQED interactions. The fundamental discrete symmetries of QED should carry over to the truncated NRQED.

Positronium energy levels have been calculated to order $m_e \alpha^6$ (Pachucki and Karshenboim, 1998; Czarnecki, Melnikov, and Yelkhovsky, 1999), and some contributions have been calculated to order $m_e \alpha^7$; see Cassidy (2018) and references therein. Experiments in positronium spectroscopy including anomalies at order 10^{-4} between precision measurements and NRQED predictions are discussed in Sec. IV.

For QED decays of positronium to photon final states, radiative corrections to the tree level processes have been

evaluated in NRQED calculations up to two loop level (Adkins, Fell, and Sapirstein, 2002). The Born term level decay rates $\Gamma(o\text{-Ps} \to 3\gamma) = 2(\pi^2 - 9)\alpha^6 m_e/9\pi$ and $\Gamma(p\text{-Ps} \to 2\gamma) = \alpha^5 m_e/2$ are multiplied by radiative correction terms of the form $\{1 + c_{nm}\alpha^n \ln^m \alpha\}$, where $n > m$ and c_{nm} are coefficients evaluated from the Feynman diagrams, presently up to $n = 3$. Branching ratios $\sim 10^{-6}$ for subleading decays of o-Ps to five photons and p-Ps to four photons are suppressed relative to the leading three- and two-photon decays by factors of $(\alpha/\pi)^2$. Radiative corrections from QCD and weak interactions as well as QED radiative corrections involving heavy leptons are small and presently beyond experimental accuracy.

The most accurate measurements of o-Ps decays are consistent with each other and with NRQED theory. Working in vacuum, Vallery, Zitzewitz, and Gidley (2003) found that

$$\Gamma = (7.0404 \pm 0.0010 \pm 0.0008) \times 10^6 \text{ s}^{-1}. \quad (8)$$

Kataoka, Asai, and Kobayashi (2009) found that

$$\Gamma = (7.0401 \pm 0.0007) \times 10^6 \text{ s}^{-1} \quad (9)$$

with the o-Ps produced in SiO_2 powder. When both the three- and five-photon contributions are included, NRQED gives the QED decay rate prediction $\Gamma = (7.039\,979 \pm 0.000\,011) \times 10^6 \text{ s}^{-1}$ (Adkins, Fell, and Sapirstein, 2002). The measurements are consistent with the NRQED theory prediction, with the caveat that the present experimental uncertainties on the decay rate are about 100 times larger than the NRQED theoretical error. The leading $\mathcal{O}(\alpha)$ correction to the decay rates is needed to agree with the data. The $\mathcal{O}(\alpha^2)$ terms are of the order of the same size as the experimental error; $\mathcal{O}(\alpha^3)$ terms are well within the experimental uncertainties, as are QCD radiative corrections.

For the p-Ps decay rate one finds that $\Gamma_p = (7989.6178 \pm 0.0002) \times 10^6 \text{ s}^{-1}$ from NRQED theory with the four-photon decay included (Adkins *et al.*, 2003), which compares with the experimental result (Al-Ramadhan and Gidley, 1994)

$$\Gamma_p = (7990.9 \pm 1.7) \times 10^6 \text{ s}^{-1}, \quad (10)$$

with the experimental error 10 000 times the size of the theoretical error within NRQED.

Going beyond QED decays to photon final states, branching ratios for possible decays involving new particles beyond the standard model are strongly constrained by precision measurements of the electron's anomalous magnetic moment, with limits on couplings of any new particles to the electron. If a new interaction were to couple to the electron with coupling α_{eff}, it would give a leading contribution to a_e of size $\alpha_{\text{eff}}/2\pi$. Taken alone, the a_e measurements imply constraints on the branching ratios of o-Ps decays to two photons plus a new light vector particle and to a photon plus new light pseudoscalar of less than 10^{-9} and 10^{-6}, respectively (Gninenko, Krasnikov, and Rubbia, 2002; Bass, 2019). Possible invisible decays of o-Ps have been sought in the context of mirror matter models of dark matter, with the branching ratio

constraint from o-Ps decays in vacuum measured to be $< 3 \times 10^{-5}$ at 90% confidence level (Vigo *et al.*, 2020).

As a bound state, positronium should inherit the symmetries of its constituents. Fundamental QED interactions encoded in the Lagrangian [Eq. (2)] respect the discrete symmetries of P, C, T, and their combinations CP and CPT, with CPT a fundamental property of relativistic quantum field theories.

The precision confirmation of QED through the electron's anomalous magnetic moment a_e implicitly implies CPT as a good symmetry for electrons, positrons, and photons. More directly, the symmetries of CPT and C have been shown to work to the level of 2×10^{-12} through measurements of $g - 2$ for both electrons and positrons (Van Dyck, Schwinberg, and Dehmelt, 1987),

$$g(e^-)/g(e^+) = 1 + (0.5 \pm 2.1) \times 10^{-12}. \quad (11)$$

For spin-1 o-Ps, CPT is tested in the three-photon decay through measurement of a CPT-odd correlation $A_{CPT} = \langle \vec{S} \cdot (\vec{k}_1 \times \vec{k}_2) \rangle$ that measures the T-odd integrated moments between the polarization vector $\vec{S}$ of the o-Ps and the momenta of the emitted photons with magnitude $k_1 \geq k_2 \geq k_3$. The most precise and recent measurement is consistent with zero with the reached precision of $\pm 0.000\,95$ (Moskal *et al.*, 2021b).

For CP symmetry the electron electric dipole moment (eEDM) puts strong constraints on any new CP violating interactions coupling to the electron. The eEDM has been precisely measured, showing that any eEDM is small (Andreev *et al.*, 2018),

$$|d_e| < 1.1 \times 10^{-29} \, e \, \text{cm}. \quad (12)$$

Equation (12) puts strong limits on new CP violating interactions coupling to the electron. If interpreted in terms of possible CP violating new heavy particle exchanges with couplings of a similar order of magnitude as standard model ones, then one finds a constraint on the new physics scale of a similar size as constraints from the LHC high-energy experiments at CERN (Andreev *et al.*, 2018). If the eEDM is instead taken to be due to the exchange of near massless particles, then one finds a bound on their coupling to the electron of $\alpha_{\text{eff}} \sim 5 \times 10^{-9}$ (Bass, 2019). Measurements of CP violating correlations involving the polarization of the o-Ps with the momentum vectors of the emitted photons are consistent with zero at $\mathcal{O}(10^{-3})$ (Yamazaki *et al.*, 2010). In future experiments, up to $\mathcal{O}(10^{-5})$ precision in CP and CPT violating correlations is expected from measurements with the J-PET tomograph in Krakow, Poland, where new correlations involving polarization of the final state photons have also been measured (Moskal *et al.*, 2016).

While the underlying QED conserves CP and CPT, finite values for CP and CPT violating correlations in o-Ps decays at the level of $\mathcal{O}(10^{-9}) - \mathcal{O}(10^{-10})$ can occur, given the fact that unstable Ps is not an eigenstate of T symmetry. These nonzero correlations are found in detailed calculations of the final state interactions, with the leading contribution coming from light-by-light scattering of two of the three photons in the final state (Bernreuther *et al.*, 1988).

To summarize, precision studies of positronium decays are consistent with QED theoretical predictions within the accuracy of present experiments. Spectroscopic measurements discussed in Sec. IV.A reveal discrepancies compared to theory that need to be understood. Positronium structure remains an interesting topic of investigation. For these measurements one needs to develop the precision methods and phenomenology of positronium production and decay in materials discussed in Sec. III. The present experimental precision on the positronium decay rates in vacuum is, however, sufficient for applications to studies in biological materials relevant to medicine discussed in Secs. V and VI.

III. POSITRONIUM PRODUCTION AND DECAY IN MATERIALS

For experiments involving tests of fundamental physics with positronium as well as in applications to medicine, one first needs to produce the positronium. How is it made? Positronium is produced via positron interactions within materials and then emitted into the vacuum and employed in fundamental physics experiments, or its decays are directly studied in medium as a function of the medium properties. In medicine one finds sensitivity to the healthiness of the tissue that the positronium is produced in.

As a first step one needs e^+ production that proceeds either via pair creation from $\gamma \to e^- e^+$ or through β^+ decays. The positrons then interact with a material and annihilate directly with electrons ($e^+ e^- \to$ photons) or make positronium that either is emitted and used in experiments or has its decay properties studied directly in medium with various processes at play that are depicted in Fig. 1 and discussed in this section. When positronium is formed it may self-annihilate or, alternatively, decay through annihilation of the positron with an electron in the medium or via intermediate reactions with

molecules in the system. One considers only the leading two-photon decays of p-Ps and three-photon decays of o-Ps for applications, with the branching ratios for the production of two extra photons suppressed by a factor of $(\alpha/\pi)^2$ and safely taken as negligible.

In this section we first outline positron production and then discuss positronium formation and decay processes in medium, with a focus on its use in fundamental physics experiments (Sec. IV) and medical applications (Sec. VI), where key media are water and mesoporous materials, materials with intermediate pores (interatomic voids) with a size in the range of 2–50 nm. Water constitutes the largest percentage of cells and in general biological materials. Mesoporous silica targets are used as efficient positron-to-positronium converters for the production and emission into vacuum of positronium for physics experiments.

A. Positron sources and positron thermalization

Positrons are routinely produced in physics and biomedical laboratories around the world via two processes: in $e^- e^+$ pair production in the electric field of the nucleus and through the use of β^+ radioactive sources (Coleman, 2003; Hugenschmidt, 2016). With $e^- e^+$ pair production, photons with energy larger than around 1.2 MeV are implanted in materials with a high atomic number Z, such as tungsten and platinum, and their energy is converted to the mass of $e^- e^+$ pairs. The high-energy photons can be generated via bremsstrahlung from decelerating electrons previously accelerated to relativistic energy by employing an electron linear accelerator; see Howell, Alvarez, and Stanek (1982), Wada *et al.* (2012), and Charlton *et al.* (2021). As an alternative, γ rays can be released from nuclear processes; see Schut *et al.* (2004), Hugenschmidt *et al.* (2008), Hawari *et al.* (2011), and Sato *et al.* (2015). With β^+ decays the starting nuclei transform into
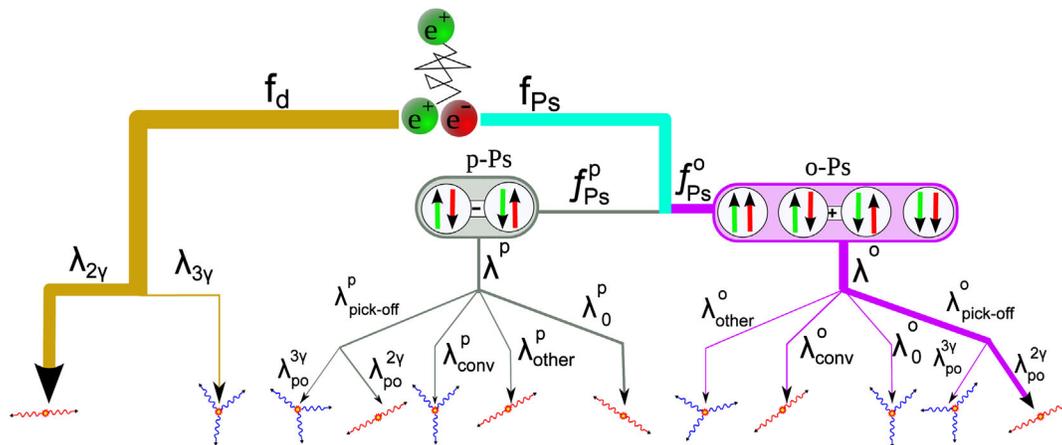
FIG. 1.   Diagram of the $e^+ e^-$ annihilation processes in matter. The scheme indicates annihilations to 2γ and 3γ only; f_d and f_{Ps} indicate fractions of direct annihilations and annihilations via positronium formation, respectively. In biological materials, a f_d/f_{Ps} ratio ranging between about $3/2$ (Harpen, 2004; Kotera, Saito, and Yamanaka, 2005) and about $1/4$ (Blanco *et al.*, 2016) has been reported. Note that f_d/f_{Ps} ratios smaller than 1 are common in mesoporous materials; see Goworek (2014). The total decay rate is due to the positronium self-annihilation (λ_0), pickoff processes (λ_{pickoff}), ortho-para conversion reactions (λ_{conv}), and other chemical processes such as oxidation (λ_{other}): $\lambda = \lambda_0 + \lambda_{\text{pickoff}} + \lambda_{\text{conv}} + \lambda_{\text{other}}$. In water $\lambda_0^p = 7990.9\ \mu s^{-1} \gg \lambda_{\text{pickoff}} = 512.8\ \mu s^{-1} \gg \lambda_{\text{conv}} + \lambda_{\text{other}} \approx 27\ \mu s^{-1}$ (O_2 saturated) $> \lambda_0^0 = 7.0401\ \mu s^{-1}$. In mesoporous silica $\lambda_0^p = 7990.9\ \mu s^{-1} \gg \lambda_{\text{conv}} \approx 25\ \mu s^{-1}$ (O_2 at 1 atm) $> \lambda_0^0 = 7.0401\ \mu s^{-1} > \lambda_{\text{pickoff}} \approx 1\ \mu s^{-1}$. Explanation is given in the text.

daughter nuclei (with atomic number Z reduced by 1) through emission of a positron and a neutrino. A large variety of β^+ radio nuclides with a half-life ranging from less than a second up to several years and maximum positron energy ranging between several hundreds of keV and a few MeV are available. The most commonly used in physical laboratories is ^{22}Na (half-life of 2.6 yr with maximum positron energy 0.54 MeV) (Hugenschmidt, 2016), while for biomedical applications there is a growing interest in ^{44}Sc (half-life of 4 h with maximum positron energy of 1.47 MeV) (Hernandez *et al.*, 2014; Rosar *et al.*, 2020; Choiński and Łyczko, 2021; Matulewicz, 2021). A ^{44}Sc radioisotope can be obtained from the ^{44}Ti/^{44}Sc generator (Filosofov *et al.*, 2010; Pruszynski *et al.*, 2010), and also by irradiation with protons or deuterons of an enriched ^{44}Ca target (Choiński and Łyczko, 2021; Mikolajczyk *et al.*, 2021). ^{44}Ti transforms to ^{44}Sc with a half-life of 60 yr via electron capture (Roesch, 2012). The long lifetime of ^{44}Ti makes the ^{44}Ti/^{44}Sc generator convenient for laboratory and clinical applications.

In the decay of ^{22}Na and ^{44}Sc radionuclides, excited daughter nuclei are produced that then deexcite through the emission of a prompt photon via the following reaction chains:

$$^{22}\text{Na} \rightarrow {}^{22}\text{Ne}^* + e^+ + \nu + \gamma(1.27 \text{ MeV}, 3.6 \text{ ps}),$$
$$^{44}\text{Sc} \rightarrow {}^{44}\text{Ca}^* + e^+ + \nu + \gamma(1.16 \text{ MeV}, 2.61 \text{ ps}). \tag{13}$$
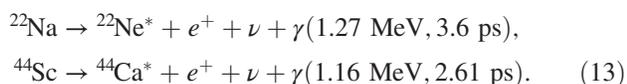
In Eq. (13) the energies of prompt photon and mean deexcitation times (Thirolf, Lang, and Parodi, 2015; Kamińska *et al.*, 2016; Choiński and Łyczko, 2021; Matulewicz, 2021) are given in parentheses.

When produced positrons are implanted in materials, they rapidly lose kinetic energy (Kubica and Stewart, 1975) in a variety of interactions (bremsstrahlung, ionization, electron excitation, phonon excitation, vibrational and rotational excitation, positronium formation, etc.) approaching the thermal energy (Schultz and Lynn, 1988; Puska and Nieminen, 1994). The efficiency of the positron stopping process depends both on the positron energy range and on the type of material, where the positron is implanted. For energies of a few tens of MeV, the dominant energy loss mechanism for positrons (as well as for electrons) is bremsstrahlung, in which the positron interacts with the Coulomb field of the nuclei and the atomic orbital electrons emitting photons (Pages *et al.*, 1972; Schultz and Lynn, 1988). At implantation energies lower than a few MeV, this energy loss mechanism becomes less efficient for positrons than for electrons due to the differing sign of the electric charge, with positrons attracted and electrons repulsed by the electric charge of the nucleus (and vice versa by the atomic electrons) (Feng, Pratt, and Tseng, 1981; Kim *et al.*, 1986).

Below several hundreds of keV (Hansen and Ingerslev-Jensen, 1983; Schultz and Lynn, 1988) down to a few electronvolts or a few tenths of an electronvolt, in the case of metals the most important energy loss processes are ionization and electron excitation (Valkealahti and Nieminen, 1983, 1984; Schultz and Campbell, 1985; Champion, 2005). In this energy range the rate of energy transfer is high (up to 10^{17}–10^{18} eV/s) and the positron energy can be reduced to a few tens of electronvolts within picoseconds (Perkins and Carbotte, 1970; Schultz and Lynn, 1988). At lower energies, electron excitation processes vanish and other mechanisms involving phonon scattering (Perkins and Carbotte, 1970; Nieminen and Oliva, 1980; Gullikson and Mills, 1986; Schultz and Lynn, 1988) and vibrational and rotational excitation processes become dominant Blanco *et al.* (2013, 2016). These last mechanisms are less efficient than the electron excitation (Dupasquier and Zecca, 1985; Schultz and Lynn, 1988). However, the complete thermalization time is estimated to be roughly 3 ps for positrons implanted with 1 keV in aluminum at a temperature of 600 K (Nieminen and Oliva, 1980). In semiconductors and insulators, where the electron excitations stop when the positron energy decreases under the band gap and a wider region of energy must be lost through phonon excitation, the thermalization results longer than in metals (Gullikson and Mills, 1986; Mills and Gullikson, 1986; Nielsen, Lynn, and Chen, 1986; Schultz and Lynn, 1988). In the case of positron implantation in water, the contribution of ionization vanishes below around 50 eV, while the contribution given by electronic excitations becomes negligible below around 7 eV (Blanco *et al.*, 2013, 2016). Vibrational and rotational excitations are expected to overcome the contribution given by other energy loss processes below around 10 eV (Blanco *et al.*, 2016). In water the entire process of thermalization takes about 5–10 ps (Stepanov, Byakova, and Stepanov, 2021), while the mean diffusion range is 1.5 and 2.1 mm for positrons from ^{22}Na and ^{44}Sc, respectively (Thirolf, Lang, and Parodi, 2015). In rare-gas solids, the absence of an optical-phonon branch further reduces the energy loss efficiency (Schultz and Lynn, 1988). As a result, positrons can diffuse for lengths of several micrometers retaining several eV of kinetic energy (Mills, Voris, and Andrew, 1994) or, in other words, positrons retain an eV energy for a few tens of picoseconds.

B. Positronium formation mechanisms

In materials with a wide energy band gap, a positron with kinetic energy less than the band gap can also lose energy in positronium formation (Schultz and Lynn, 1988). Ps formation is energetically possible if the positron energy is within the so-called Ore gap (Ore, 1949), i.e., between the ionization threshold (I) of the material and $I - 6.8$ eV (where 6.8 eV is the Ps binding energy in vacuum). This process was extensively investigated in the case of ice in the early 1980s (Eldrup *et al.*, 1983, 1985; Van House, Rich, and Zitzewitz, 1984).

In addition to this Ore mechanism with positronium formation during the process of positron thermalization, even thermalized positrons can form positronium in condensed molecular media (dielectric liquids, polymers, molecular solids, and ionic crystals). For details, see Brandt and Wilkenfeld (1975), Eldrup *et al.* (1983), Sferlazzo, Berko, and Canter (1985), Wang *et al.* (1998), and Jean, Mallon, and Schrader (2003). During the positron thermalization process, a number of positive ions, free electrons, excited molecules, and radicals are created. Freed electrons have a typical average kinetic energy of 10–50 eV (Mogensen, 1974) that thermalizes traveling for a few tens of nanometers in the material. [In ice this distance is roughly 30 nm (Eldrup *et al.*, 1983).]

Positronium can then be formed by the recombination of a thermalized electron and the thermalized positron. Two models of recombination have been introduced [the spur model by Mogensen (1974) and the blob model by Stepanov and Byakov (2002)] and successfully applied to study Ps formation in solid (Eldrup *et al.*, 1983) and liquid water (Stepanov, Byakov, and Hirade, 2007) and, more generally, in molecular liquids and polymers (Dauwe, van Waeyenberge, and de Baerdemaeker, 2005; Stepanov, Byakov, and Kobayashi, 2005). In the bulk of crystalline metals or semiconductors, this bulk formation is hindered by the presence of free electrons that screen the positron-electron interaction destroying the Ps binding (Schultz and Lynn, 1988). In such materials, positronium formation can occur only at the surface, where a thermalized positron reaching the surface picks up an electron forming Ps (Mills, Platzman, and Brown, 1978; Lynn and Welch, 1980). For unpolarized electrons and positrons forming positronium, each of the four e^+e^- spin states $|\uparrow\uparrow\rangle$, $|\downarrow\downarrow\rangle$, $|\uparrow\downarrow\rangle$, and $|\downarrow\uparrow\rangle$ are equally populated. Formation of $o\text{-Ps} = \{|\uparrow\uparrow\rangle; (1/\sqrt{2})(|\uparrow\downarrow\rangle + |\downarrow\uparrow\rangle); |\downarrow\downarrow\rangle\}$ is 3 times more probable than $\text{p-Ps} = (1/\sqrt{2})(|\uparrow\downarrow\rangle - |\downarrow\uparrow\rangle)$, so $f_{Ps}^p = 1/4$ and $f_{Ps}^o = 3/4$. In materials, o-Ps undergoes pickoff and conversion processes discussed later that shorten its lifetime relative to its decay in vacuum. In the presence of voids and open volumes (see the right panel of Fig. 2), o-Ps formed in the material can be emitted in the porosity with a kinetic energy typically corresponding to its work function that is usually on the order of a few eVs (Tuomisaari, Howell, and McMullen, 1989; Nagashima *et al.*, 1998). Thanks to its relatively long lifetime, o-Ps can lose a fraction of its energy by collisions with the

walls of the pores (Chang, Xu, and Zeng, 1987; Vallery, Zitzewitz, and Gidley, 2003). If the pores are interconnected and open to the surface (as illustrated in Fig. 2, right panel), o-Ps can diffuse along the pore network and can eventually be emitted into the vacuum with a significantly lower energy (Vallery, Zitzewitz, and Gidley, 2003; Ito *et al.*, 2005; Tanaka, Kurihara, and Mills, 2006; He *et al.*, 2007; Cassidy *et al.*, 2010; Mariazzi, Bettotti, and Brusa, 2010). The Ps emission energy into the vacuum depends on the rate and duration of the energy transfer to the surrounding material that are determined by the pore shape, pore dimension, and characteristics of the pore's surface (Nagashima *et al.*, 1995; Vallery, Zitzewitz, and Gidley, 2003; Ito *et al.*, 2005; Tanaka, Kurihara, and Mills, 2006; He *et al.*, 2007; Mariazzi, Salemi, and Brusa, 2008; Cassidy *et al.*, 2010; Crivelli *et al.*, 2010; Mariazzi, Bettotti, and Brusa, 2010; Mariazzi *et al.*, 2021). In silica Ps formation occurs with an overall positron-to-positronium conversion efficiency up to 84% (Van Petegem *et al.*, 2004). Thanks to this characteristic, in recent years efficient sources of Ps have been synthesized by exploiting either silica-based disordered porous systems (Cassidy *et al.*, 2010; Liszkay *et al.*, 2012; Consolati *et al.*, 2013) or oxidized nanochanneled silicon targets (Mariazzi, Bettotti, and Brusa, 2010; Mariazzi *et al.*, 2010). The left panel of Fig. 2 shows an image of the oxidized tunable nanochannel in silicon.

For fundamental physics experiments such mesoporous based-silica converters are used for the production of positronium and its emission into vacuum (Cassidy and Mills, 2007; Cassidy *et al.*, 2012; Wall *et al.*, 2015; Cooper *et al.*, 2016; Aghion *et al.*, 2018; Amsler *et al.*, 2019, 2021; Gurung *et al.*, 2020); see also Sec. IV. Special mesostructured based-silica thin films enable emission of positronium in transmission (forward) and in reflection (backward) relative to the direction of the positron beam (Andersen *et al.*, 2015; Mariazzi *et al.*, 2022).

FIG. 2.   Left panel: scanning electron microscope picture of the surface of a silicon positron-to-positronium converter with oxidized tunable nanochannels. From Mariazzi, Bettotti, and Brusa, 2010. Right panel: illustration of positron thermalization in mesoporous material. Ionization places on a thermalization path are shown. They are composed of electrons (−), ions (+), and positrons (blue line). In the upper example a positron thermalizes, producing free electrons that quickly thermalize. Next positronium is formed by recombination with a thermalized electron and Ps is localized in the void. After bouncing between the walls in the void (black arrows), it leaves the material. In the lower example a thermalized positron scatters in the material and annihilates directly into two photons (red arrows).

C. Direct positron annihilation in matter

A positron passing through matter may annihilate with electrons directly in flight (Weber *et al.*, 1999; Hunt *et al.*, 2001; Čížek, Vlček, and Procházka, 2012). However, owing to the fact that the cross section of annihilation is inversely proportional to the positron velocity, these annihilations represent only about 1% (Harpen, 2004; Dryzek, Suzuki, and Yu, 2007) of the total annihilation rate. At the end of the positron thermalization path, when its energy is small (on the order of tens of eV compared to its initial energy of MeV) the annihilation rate becomes large. As explained in Sec. III.B and illustrated in the right panel of Fig. 2, a positron either may form Ps or may diffuse in the material until it is directly annihilated with an electron. The average time elapsing to direct annihilation of a thermalized positron can be long. For instance, in water it is much longer than the mean lifetime of p-Ps, 125 ps, and amounts to about 400–450 ps (Eldrup and Mogensen, 1972; Kotera, Saito, and Yamanaka, 2005). The fraction of implanted positrons directly annihilating (f_d) in water has been estimated to range between ∼0.2 (Blanco *et al.*, 2016) and ∼0.6 (Harpen, 2004; Kotera, Saito, and Yamanaka, 2005). In silica, where as seen in Sec. III.B a large

amount of implanted positrons form positronium, f_d can be smaller than 0.2 (Van Petegem *et al.*, 2004; Goworek, 2014).

D. Positronium annihilation in matter

Positronium created in matter may annihilate via the processes shown in Fig. 3: (i) self-annihilation in vacuum described by the decay constant $\lambda_0^o = 7.04$ μs^{-1} for *o*-Ps and $\lambda_0^p = 7990.9$ μs^{-1} for *p*-Ps [see Eqs. (8)–(10)]; (ii) annihilation via a pickoff process where a positron from positronium annihilates with the electron from the surrounding atoms (λ_{pickoff}) [see Brandt, Berko, and Walker (1960) and Wada *et al.* (2012)]; (iii) *o*-Ps $\leftrightarrow$ *p*-Ps conversion via spin exchange reactions with paramagnetic molecules such as O$_2$ (λ_{conv}) [see Ferrell (1958), Kakimoto *et al.* (1987), Shinohara *et al.* (2001), and Cassidy *et al.* (2007)]; and (iv) other reactions such as oxidation (λ_{other}) (Stepanov *et al.*, 2009).

The total decay rate is then expressed as $\lambda^{p(o)}(t,C) = 1/\tau_0^{p(o)} = \lambda_0^{p(o)} + \lambda_{\text{pickoff}}(t) + \lambda_{\text{conv}}(C) + \lambda_{\text{other}}(C)$, with dependence on time t and concentration of dissolved molecules C. The pickoff rate is decreasing in time and conversion, and other chemical reactions depend on the concentration of dissolved molecules. In the biological samples, by analogy to water, the self-annihilation rate of *p*-Ps ($\lambda_0^p = 7990.9$ μs^{-1}) is much larger than the pickoff rate ($\lambda_{\text{pickoff}} = 512.8$ μs^{-1} in water), which in turn is much larger than the conversion and other reaction rate ($\lambda_{\text{conv}} + \lambda_{\text{other}} \approx 27$ μs^{-1} in O$_2$ saturated water), which is larger than the *o*-Ps self-annihilation rate ($\lambda_0^0 = 7.0401$ μs^{-1}). In porous materials the relation changes
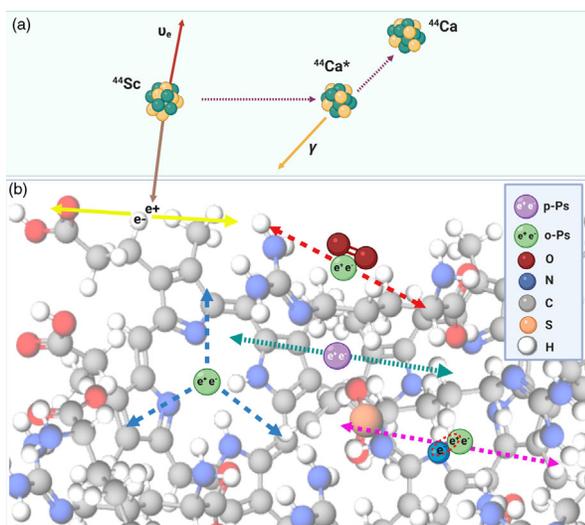
FIG. 3. (a) Decay of a ^{44}Sc isotope; see Eq. (13). (b) Illustration of the basic processes leading to the annihilation of a positron in the intramolecular voids of a hemoglobin molecule. The most probable ways of annihilation are direct annihilation into two photons (yellow solid arrows), with the positron originating from the ^{44}Sc decay, self-annihilation of *p*-Ps (green dotted arrows), self-annihilation of *o*-Ps (blue dashed arrows), *o*-Ps pickoff process (violet dotted arrows), and *o*-Ps conversion on an O$_2$ molecule (red dashed arrows). The distances and the size of the atoms are shown to scale, with the diameter of positronium twice that of hydrogen.

and $\lambda_{\text{conv}} \approx 25$ μs^{-1} (O$_2$ at 1 atm) $> \lambda_0^0 = 7.0401$ μs^{-1} $> \lambda_{\text{pickoff}} \approx 1$ μs^{-1}. More details are given in the caption of Fig. 1 and in Secs. III.D.1 and III.D.2.

1. Annihilation via the pickoff process

The annihilation rate via the pick-off process (λ_{pickoff}) may be treated as independent of the positronium spin, with the same value for *o*-Ps and *p*-Ps ($\lambda_{\text{pickoff}}^o = \lambda_{\text{pickoff}}^p$) (Dupasquier, De Natale, and Rolando, 1991), and expressed as $\lambda_{\text{pickoff}} = \xi[(1/4)\lambda_0^p + (3/4)\lambda_0^o] \approx \xi[(1/4)\lambda_{2\gamma} + (3/4)\lambda_{3\gamma}]$. Here ξ denotes the positron-electron contact density normalized with respect to the vacuum value, while λ_0^p and λ_0^o denote self-annihilation rate of *p*-Ps and *o*-Ps, respectively. The fractions 1/4 and 3/4 originate from the spin projection combinations, as explained earlier, while $\lambda_{2\gamma}$ and $\lambda_{3\gamma}$ denote the decay rate into two and three photons, respectively. Assuming to good approximation that *p*-Ps self-annihilates to 2γ and *o*-Ps annihilates to 3γ, the relative rate of 3γ and 2γ pickoff annihilations is $3\lambda_{3\gamma}/\lambda_{2\gamma} \approx 3\tau_{p\text{-Ps}}/\tau_{o\text{-Ps}} \approx 1/378$, where $\tau_{p\text{-Ps}}$ and $\tau_{o\text{-Ps}}$ denote the mean lifetime of *p*-Ps and *o*-Ps, respectively. The rate constant for pickoff annihilation ranges from a fraction of a μs^{-1} in some mesoporous materials (Saito and Hyodo, 1999; Jasinska *et al.*, 2016) to about $\lambda_{\text{pickoff}}^{\text{water}} = 513$ μs^{-1} $- 550$ μs^{-1} in water (Shibuya *et al.*, 2020; Stepanov *et al.*, 2020). The value of 513 μs^{-1} is small compared to the self-annihilation rate constant of *p*-Ps ($\lambda_0^p = 7990.9$ μs^{-1}). Therefore, the *p*-Ps mean lifetime τ^p is shortened due to pickoff only by about a few picoseconds $[\tau_0^p - \tau^p = 1/7990\,\mu\text{s}^{-1} - 1/(7990\,\mu\text{s}^{-1} + 513\,\mu\text{s}^{-1}) \approx 7\,\text{ps}]$. In contrast, the self-annihilation rate of *o*-Ps with $\lambda_0^o = 7.0401$ μs^{-1} is much smaller than the pickoff rate in liquids and the *o*-Ps mean lifetime is significantly shortened: down to 1.8 ns in water compared to 142 ns in vacuum. In mesoporous materials the pickoff rate constant depending on the structure is of the order of 1 μs^{-1}. It decreases the *o*-Ps mean lifetime by tens of nanoseconds. For example, for the IS3100 aerogel with $\tau_{o\text{-Ps}} = 132$ ns (Jasinska *et al.*, 2016), one finds $\lambda_{\text{pickoff}}^o = 1/\tau_{o\text{-Ps}} - \lambda_0^o \approx 0.6$ μs^{-1}. It is important to emphasize that the pickoff annihilation rate is not constant in time. As mentioned in Sec. III.B and illustrated in Fig. 2, positronium after formation is bouncing between the void's walls losing its energy, and hence slowing down. Therefore, the average time intervals between subsequent positronium interactions with electrons from surrounding molecules are growing and the pickoff rate decreases in time. Experimentally, this may be controlled by determining the time dependence of the ratio of the 3γ (self-annihilation) to 2γ (pickoff annihilation).

2. Positronium conversion and oxidation

Positronium in matter takes part in chemical reactions with radiolytic products (solved in water as aqueous electrons, H$_3$O$^+$, OH radicals, etc.) created by the positron during thermalization and in reactions with dissolved substances (Stepanov, Byakov, and Hirade, 2007; Stepanov *et al.*, 2020). Interaction of positronium with dissolved paramagnetic molecules possessing magnetic moment, such as molecular oxygen (O$_2$), may lead to the spin exchange and conversion of

p-Ps into *o*-Ps and *o*-Ps into *p*-Ps, for instance, via the $o\text{-Rs} + O_2 \rightarrow p\text{-Rs} + O_2$ reaction (Ferrell, 1958; Kakimoto *et al.*, 1987; Shinohara *et al.*, 2001; Stepanov *et al.*, 2020). (Such nonparamagnetic molecules as N_2 are not causing conversion reactions.) In addition the O_2 molecule may also oxidize positronium via the $\text{Rs} + O_2 \rightarrow e^+ + O_2^-$ process. Both processes, *o*-Ps conversion and oxidation, contribute to the quenching of *o*-Ps. Conversion in some organic liquids (cyclohexane, isooctane, and isopropanol) is 5–10 times more frequent than oxidation (Stepanov *et al.*, 2020). The conversion and oxidation rate constants depend on the dissolved oxygen concentration C_{O_2}: $\lambda_{conv} + \lambda_{other} = k_{O_2} C_{O_2}$, with the value k_{O_2} for water measured to be 0.0204 ± 0.0008 $\mu\text{mol}^{-1}\,\mu\text{s}^{-1}\,\text{l}$ (Shibuya *et al.*, 2020) and 0.0186 ± 0.0010 $\mu\text{mol}^{-1}\,\mu\text{s}^{-1}\,\text{l}$ (Stepanov *et al.*, 2020). This gives $\lambda_{conv} + \lambda_{other} \approx 27$ μs^{-1} with saturated O_2 in water ~ 1400 $\mu\text{mol}\,\text{l}^{-1}$. Thus, the conversion rate depends linearly on the dissolved O_2 concentration. In mesoporous materials at relatively low concentrations (< 0.05 atm), it exceeds the pickoff rate. On the other hand, at 0.25 atm it exceeds the self-annihilation rate of *o*-Ps (Zhou *et al.*, 2015). In water the conversion rate is much lower than the pickoff rate, but in some organic liquids with high oxygen solubility it may become the dominant effect (Stepanov *et al.*, 2020). The main annihilation processes of the thermalized positron in a molecule of hemoglobin, which is the most important component of red blood cells (erythrocytes), an example relevant for the medical applications discussed in Sec. VI, is shown in Fig. 3.

IV. FUNDAMENTAL PHYSICS EXPERIMENTS WITH POSITRONIUM

In the last few decades, the development of techniques for trapping many positrons and forming bunches containing up to several 10^7 positrons (Surko, Leventhal, and Passner, 1989; Murphy and Surko, 1992; Cassidy, Deng, and Greaves, 2006; Danielson *et al.*, 2015) and the development of efficient positron-to-positronium converters (see Sec. III) are facilitating significant advancements in the field of experimental positronium physics (Cassidy, 2018). This includes experiments with positronium spectroscopy, tests of gravity on antimatter, and production of a positronium Bose-Einstein condensate.

A. Positronium spectroscopy

Positronium spectroscopy presently focuses on precision measurements of hyperfine transitions between singlet and triplet states (Cassidy, 2018). Today hyperfine splittings in positronium are measured to the megahertz level, whereas the theoretical NRQED calculations are typically at the kilohertz level. There are several interesting discrepancies at the few standard deviation level between measurements of hyperfine splittings and NRQED predictions (Adkins, Cassidy, and Pérez-Ríos, 2022).

Early measurements of the frequency of the $1S$ hyperfine interaction (Mills, 1983; Ritter *et al.*, 1984) are about 3 standard deviations below the theoretical NRQED predictions (Adkins, Fell, and Mitrikov, 1997; Hoang, Labelle, and Zebarjad, 1997; Czarnecki, Melnikov, and Yelkhovsky, 1999), or about 1 part in 10^5. More recent measurements were reported by Ishida *et al.* (2012, 2014) and Miyazaki *et al.* (2015), with the first closest to the theoretical prediction (within 1.2 standard deviations). These results have raised discussion about possible systematics in the experiments (Heiss *et al.*, 2018) and the theory and contributing Feynman diagrams (Karshenboim, 2004).

Motivated by the situation with the $1S$ splitting, the ETH Zürich group are planning an in-vacuum precision measurement to look at the $2^3S_1 \rightarrow 2^1S_0$ transition and to compare with NRQED predictions. This new experiment will be free of the systematic uncertainties that were inherent in previous $1S$ HFS transition measurements (Heiss *et al.*, 2018).

Most recently Gurung *et al.* (2020, 2021) measured the $2^3S_1 \rightarrow 2^3P_0$ transition on Ps emitted into vacuum from mesoporous silica targets and determined the transition frequency $\nu_0 = 18\,501.02 \pm 0.61$ MHz. This value differs from the NRQED prediction $\nu_0 = 18\,498.25 \pm 0.08$ MHz, where the quoted theoretical error includes an estimate of unknown higher order NRQED corrections. The difference is about 1 part in 10^4, a 4.5σ effect.

The interesting status of these measurements and their relation to theory calls for new experiments. If there are no underestimated systematics in the experiments given the constraints on possible new interactions coupling to the electron discussed in Sec. II, then attention will turn to QED bound state theory. What from QED might be missing from present NRQED calculations? Assuming no large extra diagrams waiting to enter at next order, one might consider the input assumptions to the NRQED bound state calculations. One effect might be a slightly underestimated harder momentum distribution of electron velocities in the positronium wave functions, for instance, on external lines. Alternatively, one might consider enhanced Ps resonance contributions as admixtures in the self-energy diagrams for excited states.

B. Positronium in gravity tests and Bose-Einstein condensates

Going beyond positronium spectroscopic and decay measurements, positronium also plays an important role in other fundamental physics experiments: tests of the equivalence principle through the effect of gravity on antimatter and possible Bose-Einstein condensates involving antimatter. To measure the effect of gravity on antimatter, on the one hand, *o*-Ps in excited states is being used by two experiments at CERN's Antiproton Decelerator, AEgIS (Doser *et al.*, 2018) and GBAR (Perez and Sacquin, 2012; Dufour *et al.*, 2015), as an intermediate tool to produce antihydrogen via a charge-exchange reaction with antiprotons (Amsler *et al.*, 2021). The goal of these experiments is to measure the acceleration experienced by antihydrogen in the gravitational field of Earth. The cross section of the charge-exchange reaction for a high value of the principal quantum number of *o*-Ps is expected to scale with the fourth power of the principal quantum number itself (Krasnicky *et al.*, 2016). Consequently, production of antihydrogen via a charge-exchange reaction will take benefit from the efficient laser excitation to Rydberg states demonstrated in the last decade on *o*-Ps emitted into

vacuum from silica-based converters (Cassidy *et al.*, 2012; Wall *et al.*, 2015; Aghion *et al.*, 2016). On the other hand, long-lived positronium states have been proposed as probes for direct measurements of gravity on a matter-antimatter system (Mills and Leventhal, 2002; Oberthaler, 2002; Mariazzi *et al.*, 2020). *o*-Ps excited both to Rydberg states (Cassidy *et al.*, 2012) and to the metastable 2^3S level (Amsler *et al.*, 2019) has been proposed for such measurements.

Orthopositronium has the potential to form a Bose-Einstein condensate (BEC) at high densities (Platzman and Mills, 1994) that, if observed, would be the first BEC involving antimatter with the experiments also providing information about high density *o*-Ps collisions and possible *o*-Ps molecule formation.

A recent suggestion (Mills, 2019) involved taking a hollow spherical bubble containing thousands of spin-aligned *o*-Ps atoms in superfluid liquid ^{4}He. The bubble would be stable against breakup into smaller bubbles, and the Ps would form a BEC with a number density of $\sim 10^{20}$ cm^3 and a BEC critical temperature $T_c \approx 300$ K. With present experimental methods bubbles might be formable, containing about 10^5 *o*-Ps atoms.

For a BEC involving spin flip from *o*-Ps to *p*-Ps, the spontaneous radiation of positronium atoms in the BEC due to the two-photon collective annihilation decay might be used as an intense γ-ray source (Avetissian, Avetissian, and Mkrtchian, 2014). Owing to BEC coherence the number of emitted photons will grow at every place in the condensate. For laser production with direction focused radiation, an elongated condensate might be used. Spontaneously emitted entangled and opposite directed photon pairs will be amplified, leading to an exponential buildup of a macroscopic population into end-fire modes in the elongated condensate.

C. Photon entanglement in positronium decays

Quantum entanglement of the emitted photons in positronium decays is an interesting fundamental physics issue (Acin, Latorre, and Pascual, 2001; Hiesmayr and Moskal, 2017; Nowakowski and Bedoya Fierro, 2017). It also has interesting applications in PET devices for medical diagnostics (McNamara *et al.*, 2014; Toghyani *et al.*, 2016; Moskal *et al.*, 2018; Caradonna *et al.*, 2019; Hiesmayr and Moskal, 2019; Watts *et al.*, 2021). Thus far the entanglement of photons from positronium, though predicted by theory, has not been experimentally observed. Implementation of such an experiment is challenging since the polarization of photons in the MeV energy range cannot be studied using optical methods.

Photons are spin-1 particles characterized by their momentum and polarization, with two transverse polarization states for real photons. In the linear polarization basis, the 2γ state $|\psi\rangle$ originating from *p*-Ps can be written as

$$|\psi\rangle = \frac{1}{\sqrt{2}}(|H\rangle_1 \otimes |V\rangle_2 - |V\rangle_1 \otimes |H\rangle_2), \qquad (14)$$

where $|H\rangle$ and $|V\rangle$ denote the horizontal and vertical polarized states, and the symbol $\otimes$ refers to a tensor product. The minus sign between the two combinations reflects the parity -1 eigenvalue of ground state positronium. The entanglement of
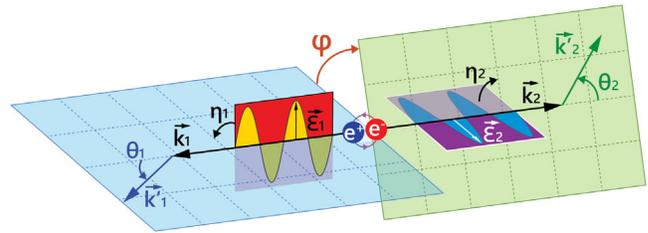
FIG. 4. Schematic of Compton scattering of two photons originating from *p*-Ps annihilation. Owing to the momentum conservation ($\vec{k}_1 = -\vec{k}_2$), the annihilated photons propagate back to back along the same axis in the *p*-Ps rest frame. θ_1 and θ_2 denote the scattering angles, η_1 and η_2 denote the angles between the scattering planes and the polarization directions $\vec{e}_1$ and $\vec{e}_2$, respectively, and φ indicates the relative angle between the scattering planes.

the 2γ state described in Eq. (14) manifests itself in the fact that there is no choice of basis ($|A\rangle$ or $|B\rangle$) in which the state could be described by the single tensor product of $|A\rangle \otimes |B\rangle$: we call this entanglement. Moreover, Bose symmetry and parity conservation in the decay of *p*-Ps imply that the state of the resulting two photons is maximally entangled and that the photons' polarizations are orthogonal to each other: $\vec{e}_1 \perp \vec{e}_2$ (Hiesmayr and Moskal, 2019). Photons in the MeV energy range interact in matter predominantly with electrons through photoelectric and Compton effects. Compton scattering (Fig. 4) may be used for an estimation of the linear polarization of the incoming photon since the scattering is not isotropic and it is most probable in the plane perpendicular to the polarization of the incoming photon (Klein and Nishina, 1929). For the *p*-Ps $\to 2\gamma$ process (Fig. 4), when each γ interacts via Compton scattering with an electron one can estimate the angle between the polarization directions of the photons $|\eta_1 - \eta_2|$ by measurement of the relative angle φ between the scattering planes (Moskal *et al.*, 2018). The distribution of φ may serve for studies of quantum entanglement (Hiesmayr and Moskal, 2019). The experimentally determined distributions (Moskal, 2018; Watts *et al.*, 2021; Abdurashitov *et al.*, 2022) indeed peak for $\varphi = 90°$ and are consistent with predictions obtained under the assumption that photons are entangled. However, to prove the entanglement of photons from *p*-Ps, measurements in at least two different bases are required (Hiesmayr and Moskal, 2019), for instance, $(|H\rangle, |V\rangle)$ and $(|+45°\rangle, |-45°\rangle)$. Yet, the researcher has no influence on Compton scattering and an active basis choice cannot be realized. Therefore, thus far the experimental challenge of proving the entanglement of photons from positronium decays remains open. However, the strong correlation between the photon's polarization may be applied in medical diagnostics, as discussed in Sec. VI.D.

V. DEVELOPMENT OF POSITRONIUM RESEARCH IN BIOLOGY AND MEDICINE

As discussed, the predictions of positronium properties based on NRQED theory are currently many orders of magnitude more precise than the experimental results.

Experimental precision is to a large extent limited because positronium is produced in medium, and its properties in materials are altered with respect to the vacuum. Yet, the variation of positronium properties as a function of the nanostructure of the material and the concentration in it of paramagnetic molecules constitute the basis for its application in studies of materials, as well as in studies of biological processes in living organisms and potentially also in medicine.

Although positron-emitting radionuclides have been used in diagnostic medicine since Kuhl and Edwards (1963) developed the foundations of medical PET in the late 1950s, the properties of the positronium atom were not used in medicine until recently. Recent advances in developing multiphoton tomography (Moskal *et al.*, 2021b) and imaging of positronium properties (Moskal *et al.*, 2021a) opened realistic perspectives making use of positronium as a diagnostic indicator of the tissue pathology in clinics (Moskal and Stępień, 2022).

In this section we explain how positronium can help in understanding the structure of biological objects, how positronium is used in life science, and why its properties should be translated to medicine. The method used for the studies is called positron annihilation lifetime spectroscopy (PALS) and is based on the measurement of positron lifetime spectrum in the investigated sample. The positron may be implemented in the sample using a positron beam or through the application of β^+ radionuclides such as ^{22}Na or ^{44}Sc. Typically in the PALS method two scintillation detectors are used. One detector is employed for determining the time of the annihilation photon originating from the electron-positron annihilation, and the other is used to determine the time when the positron enters the sample that is established by the measurement of a prompt gamma photon emitted by the excited daughter nucleus described in Eq. (13). The measured lifetime spectra enables one to extract the intensities and mean lifetime distributions of positrons undergoing annihilations due to various processes depicted in Fig. 1.

The first measurements of intensity ($I_{o\text{-Ps}}$) and the mean lifetime ($\tau_{o\text{-Ps}}$) of o-Ps were performed on samples containing organic compounds, benzene derivatives. This experiment showed significant differences in the signal intensity (I) in the presence of halogen atoms (F, Cl, Br, and I), which was explained by the increased electron density of such molecules (Hatcher, Millett, and Brown, 1958). An attempt in those studies was made to find a relation between the mean lifetime and the dissociation energy of the molecular bonds in simple organic compounds, and no suggestion was then given that the functional groups, similar to those organic compounds, might affect the average lifetime of o-Ps ($\tau_{o\text{-Ps}}$) in biological samples (Kerr and Hogg, 1962; Brown, 1974). Immediately after finding positronium properties in organic fluids, Gustafson (1970) measured $\tau_{o\text{-Ps}}$ in a biological sample (muscle). However, he focused his attention on the order and arrangement of tissue water and not on muscle structure. Further studies on complex biological systems like biological membranes or proteins moved positronium research toward structural biology and showed that this approach was efficient in the study of biological reactions [such as electron transfer (Jean and Ache, 1977)], phase transition of lipids (Stinson

et al., 1980; Chow, Chuang, and Tseng, 1981; Jean and Hancock, 1982), macromolecule structure (Handel, Graf, and Glass, 1976), hydratation (Handel, Graf, and Glass, 1980; Gregory, Chai, and Su, 1992; Akiyama *et al.*, 2007), and porosity (Pamula, Dryzek, and Dobrzynski, 2006; Chamerski *et al.*, 2017) of biological samples. After many years of focused research, PALS now appears to be a promising technique in the investigation of the structure of macromolecules (Chen, van Horn, and Jean, 2012) and clinical samples (Zgardzinska *et al.*, 2020; Moskal *et al.*, 2021a, 2023; Avachat *et al.*, 2022).

A. Positronium in biological materials and systems

The first applications of positronium properties in the life sciences were made by Handel, Graf, and Glass (1976, 1980) in the late 1970s. Keeping in mind that the positron annihilation lifetime is sensitive to changes in free volume caused by pressure (which is rarely studied in biological systems) or by thermal expansion in the same phase, they showed significant changes in positronium lifetime during the phase transitions of the biological systems. Covalent bonds between carbon atoms in organic molecules hold structure (architecture) of biological macromolecules contributing to the creation of free volumes (so-called molecular voids). This molecular structure [called the nanostructure here (Pethrick, 1997)] is changing dynamically with temperature (Handel, Graf, and Glass, 1976; Stinson *et al.*, 1980; Sane *et al.*, 2009) and is stabilized by hydrogen bonds (Handel, Graf, and Glass, 1980; Gregory, Chai, and Su, 1992; Kilburn *et al.*, 2006). The specific feature of the shortening of $\tau_{o\text{-Ps}}$ in the pickoff process has been proposed for probing subnanometer-sized local free volumes in solid materials and organic polymers to assess the size and nature of the chemical environment (Pethrick, 1997; Dlubek, Fretwell, and Alam, 2000). Positronium mesurements in biological samples have been performed with a liquid ^{22}Na source (such as a NaCl solution) prepared in a thin-walled glass bead (Handel, Graf, and Glass, 1976) sealed between thin mylar films (Chow, Chuang, and Tseng, 1981), Al foil (Jean and Ache, 1977; Jean and Hancock, 1982) sealed between a Kapton foil (Stinson *et al.*, 1980; Gregory, Chai, and Su, 1992; Pamula, Dryzek, and Dobrzynski, 2006; Bura *et al.*, 2020; Moskal *et al.*, 2023), or directly dissolved as an open source (Sane *et al.*, 2009).

In life sciences two types of biomaterials, hydrogels and biomembranes, were studied intensively to characterize molecular structure (porosity, permeability, and hydrophobicity) in the context of their biological activity (Pamula, Dryzek, and Dobrzynski, 2006; Sane *et al.*, 2009). Various aspects of PALS applied to life sciences are discussed in the review by Chen, van Horn, and Jean (2012), which summarized recent knowledge about possible application of o-Ps in biology.

Fluidity and regularity of biological membranes change depending on the phospholipids (for instance, palmitoyl-oleoyl-glycero-phosphocholine) and cholesterol content, which can be observed as changes in $\tau_{o\text{-Ps}}$. For example, if cholesterol content is at the high value of 40% and dipalmitoylphosphatidylcholine (DPPC) is 60%, $\tau_{o\text{-Ps}}$ reaches the lowest value of ~1.86 ns (Sane *et al.*, 2009). Admixture of

ceramides and cholesterol ceramide interactions in DPPC membranes also influence $\tau_{o\text{-Ps}}$ by changing the free volume void pattern (Axpe *et al.*, 2015; García-Arribas *et al.*, 2016). The slope of $\tau_{o\text{-Ps}}$ rises rapidly where the membrane undergoes a gel-fluid transformation at the transition temperature of the lipid systems (Jean and Hancock, 1982; Sane *et al.*, 2009) and biological membranes (red cell ghosts) (Chow, Chuang, and Tseng, 1981). In contrast to lipid systems, where membrane permeability is regulated by lipid fluidity (Sane *et al.*, 2009), in hydrogels interaction between polymers and water is a crucial process regulating their biological activity (Sane, Toumisto, and Holopainen, 2011). This process can be successfully studied by means of PALS (Pamula and Dryzek, 2008). The dehydration process in crystallized and amorphous state of macromolecules (trehalose) is marked significantly by sharp changes in the mean $\tau_{o\text{-Ps}}$ and intensity, which are related to changes in the total free volume fraction (Kilburn *et al.*, 2006).

B. Positronium in *ex vivo* research

The first experiment on a biological sample was performed in 1970 and dedicated to studying semicrystaline structure of water in muscle cells (Gustafson, 1970; Chen, van Horn, and Jean, 2012). However, the pioneering experiments on *ex vivo* samples showing that small temperature variations cause detectable changes in free voids were done on bovine liver and rabbit muscle (Elias, Al-Mashhadani, and Al-Shiebani, 2001). To develop technical details of *o*-Ps measurements, a number of experiments were performed on human and mice skin to study differences in the mean $\tau_{o\text{-Ps}}$ of normal cells and cancer (basal cell carcinoma and squamous cell carcinoma) (Jean *et al.*, 2006, 2007). This approach appeared to be promising and indicated a reduction of free volume at the molecular level for the skin with cancer, while the number of patients was the limitation to conclude about usefulness of positronium imaging in cancer diagnostics (Liu *et al.*, 2007). Extending these studies to skin melanoma showed that positrons annihilate at a smaller rate with an increase in melanoma cells, which confirmed *o*-Ps utility in biomedical research (Liu *et al.*, 2008). In addition to human and animal tissues, unicellular organisms and multicellular tissuelike structures (spheroids) were investigated, giving promising results in positronium research (Axpe *et al.*, 2014; Kubicz *et al.*, 2015; Karimi *et al.*, 2020). Positronium annihilation in tissues strongly depends on water content. In highly hydrated organs (lens) or tissues (myoma), the mean *o*-Ps lifetime is below or around ∼2 ns (Sane *et al.*, 2010; Zgardzinska *et al.*, 2020). In adipose tissue this time is significantly increased (Moskal *et al.*, 2021a, 2023; Avachat *et al.*, 2022), confirming the observation from biological systems that structural characteristic and molecular composition determine positronium annihilation.

VI. MEDICAL APPLICATIONS OF POSITRONS AND POSITRONIUM

Noninvasive imaging of the interior of the body constitutes a powerful diagnostic tool enabling personalized and targeted therapy. Here we report on tomographic methods based on positron and positronium annihilations inside living organisms. We begin with a description of PET, which is a well established diagnostic method delivering information about the metabolism rate of administered pharmaceuticals, and about receptor expression on cell membranes (Humm, Rosenfeld, and Del Guerra, 2003; Conti, 2009; Vanderberghe, Moskal, and Karp, 2020; Alavi *et al.*, 2021). PET is based on the administration to the living organism of pharmaceuticals labeled with positron-emitting isotopes, for example, fluoro-deoxy-glucose (FDG) labeled with ^{18}F and prostate specific membrane antigen labeled with ^{68}Ga for metabolic and receptor imaging, respectively (Moskal and Stępień, 2020). The image of the annihilation density distribution is reconstructed based on the registration of 2γ events originating mostly from direct annihilations, *p*-Ps self-annihilations, and *o*-Ps pickoff processes (Fig. 1). The reconstructed annihilation density distribution corresponds to the image of the metabolic rate (glucose taken by a cell) or the image of cancer cell expression (density of cancerous receptor on a cell), depending on the administered radiopharamaceuticals. In 2019 the first total-body PET systems were introduced to clinics that enable dynamical imaging (filming) of all organs and tissues in the body simultaneously (Badawi *et al.*, 2019; Karp *et al.*, 2020; Surti, Pantel, and Karp, 2020; Vanderberghe, Moskal, and Karp, 2020). Thus far PET detectors have reconstructed only annihilation position distribution. Only recently the method of *positronium imaging* was developed. It enables one to image in the living organisms properties of positronium such as a mean lifetime, production intensity, and the 3γ-to-2γ decay rate ratio (Moskal, 2019; Moskal *et al.*, 2019, 2020). Positronium imaging requires multiphoton tomography systems enabling not only registration of electron-positron annihilations into two photons (as in standard PET) but also decays to three photons, as well as simultaneous registration of annihilation photons and a prompt photon from the radionuclide deexcitation. These tomography systems as well as three-photon and mean lifetime image reconstruction methods were recently demonstrated by the J-PET Collaboration (Moskal *et al.*, 2021a, 2021b). The first *ex vivo* positronium images of healthy and cancer tissues were published by Moskal *et al.* (2021a). The *o*-Ps mean lifetime (Sec. III) tells one about the size of intramolecular voids (free volumes between atoms), whereas its formation probability (production intensity) informs one about the void concentration. Both lifetime and production intensity depend on the bioactive molecule concentration. Notably positronium may serve as a biomarker for the assessment of tissue pathology (Moskal, Jasinska *et al.*, 2019; Moskal *et al.*, 2021a, 2023) and may be of particular diagnostic relevance as a biomarker of the concentration of oxygen (Moskal and Stępień, 2021) (Sec. VI.C). We stress that positronium mean lifetime imaging delivers information complementary to the metabolic and receptor PET images and is also complementary to anatomic (electron density distribution) and morphological (hydrogen atom density distribution) images achievable with computed tomography and magnetic resonance tomography, respectively.

A. Positron emission tomography

Healthy tissue and cancerous tissue differ in the expression profile of receptors at the cell membranes, in the angiogenesis resulting in different concentrations of oxygen molecules, and in the glucose metabolism rate. We next explain how a cancer cell, which needs more glucose for its metabolism and unlimited divisions or has the vastness of cancerous receptors on its surface, can be distinguished using PET scans from a healthy cell, which is rather modest in its needs and behavior.

The number of PET scans has doubled within the last ten years, reaching around 2 000 000 PET scans per year in the U.S. (2017) and 45 000 in Poland (2016) (Cegła and Piotrowski, 2021). Typically and most commonly, ^{18}F-FDG is used as a positron-emitting compound (radiopharmaceutical) in PET for testing cancer and brain metabolism. This radiotracer was developed and first tested in humans for imaging cerebral glucose metabolism in 1976 at the University of Pennsylvania (Reivich *et al.*, 1979; Alavi and Reivich, 2002; Alavi *et al.*, 2021) and is still used in around 90% of PET scan examinations. FDG is a glucose analog, where at the second carbon atom in a glucose ring (*C*2), the normal hydroxyl group (−OH) is substituted with the ^{18}F isotope. The half-life of the ^{18}F isotope is 110 min, which makes ^{18}F-FDG a useful radiopharmaceutical in the diagnosis of disease processes characterized by increased glucose consumption, primarily in neoplastic diseases, for the assessment of brain metabolism or myocardial viability, in drug-resistant epilepsy, and for the diagnoses of Alzheimer's disease spectrum, inflammatory processes, and systemic diseases (Lin and Alavi, 2019; Alavi *et al.*, 2021). After administration via intravenous injection, FDG is distributed through the bloodstream within minutes and is actively transported into the cells by specific glucose transporters: membrane proteins that contribute in glucose uptake [mostly GLUT1 and GLUT3 (Marom *et al.*, 2001; Avril, 2004)]. Normally, once phosphorylated, a glucose molecule continues along the glycolytic pathway (glycolysis) for energy production. However, FDG cannot undergo glycolysis, because the ^{18}F atom is substituted for the −OH group. Only after ^{18}F decays radioactively, fluorine at the *C*2 position is converted to ^{18}O. After picking up a proton (H$^+$) from a hydronium ion (H$_3$O$^+$) in its aqueous environment, the FDG molecule becomes a glucose-6-phosphate labeled with harmless non-radioactive "heavy oxygen" in the −OH group at the *C*2 position that is ready to be metabolized in the cell (Królicki and Kunikowska, 2021). Another approach used for PET imaging applies a radiotracer for direct labeling of a target cell. In breast cancers approximately 20%–30% of cases overexpress the HER2 receptor (human epidermal growth factor receptor family), which results from HER2-gene amplification (Rubin and Yarden, 2001; Sawyers, 2019). In around 90% of HER2-positive cancer cells, up to several hundred HER2-gene copies are generated to produce over 100 times more protein receptors in a cancer cell relative to a healthy cell (Venter *et al.*, 1987; Zabaglo *et al.*, 2013). This makes the HER2 protein a suitable and ideal biomarker for treatments and diagnosis of HER2-positive cancer in not only breast cancer but also in gastric, bladder, pancreatic, and

ovarian cancers (Yan *et al.*, 2015; Sawyers, 2019). Several groups of molecules targeting HER2 have been developed for molecular imaging with radiotracers used in PET. Among them, the designed humanized monoclonal antibody against HER2 protein (trastuzumab) has been used in multiple clinical trials (Henry, Ulaner, and Lewis, 2018). Currently clinical trials with HER2 targeting radiotracers use radionuclides emitting additional prompt γ during β^+ decay, which would enable determination of the positronium mean lifetime,
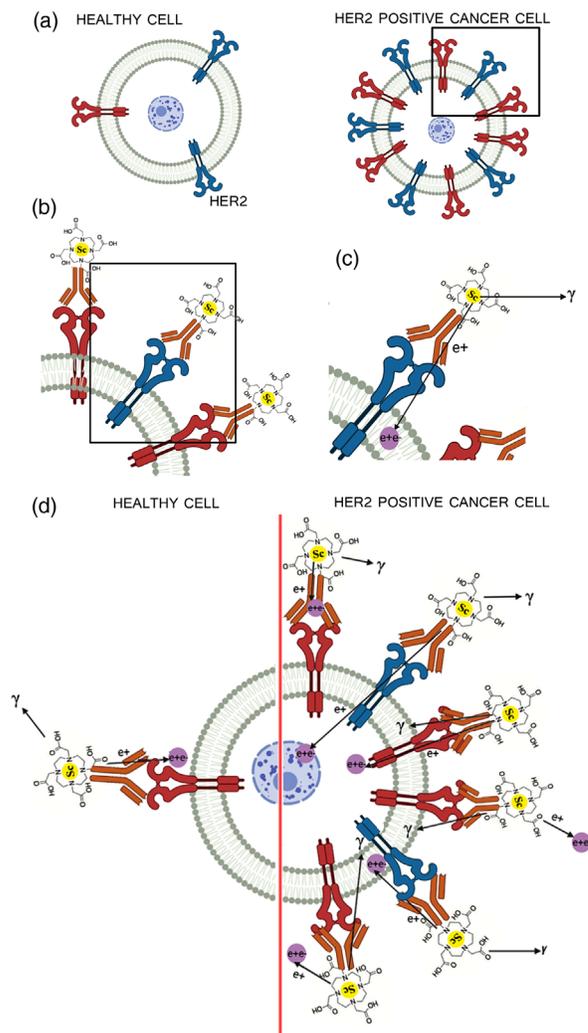
FIG. 5. Positronium imaging of HER2-positive cancer cells. (a) The HER2 receptor (epidermal growth factor receptor) is scarcely expressed on the surface of healthy cells and significantly (100 times or more) overexpressed in cancer cells [such as breast cancer (Venter *et al.*, 1987; Rubin and Yarden, 2001)]. Different colors represent combinations of different units forming dimmers of the HER2 molecule. (b) Trastuzumab (herceptin), a humanized monoclonal antibody that binds to HER2, is labeled as a ^{44}Sc isotope. (c) ^{44}Sc isotope emits a prompt γ and a positron (e^+) to form a positronium atom. (d) Positronium atoms annihilate in cells (with highest abundance in cancer), on their surface and within cell organelles (cell membranes and cytosol nuclei). Environmental factors like temperature, water content, and other specific tissue features like chemical and molecular composition determine $\tau_{o\text{-Ps}}$ in the diagnosed tissue.

as recently proposed by Moskal and Stępień (2020). Using $\beta^+\gamma$ emitters for targeting HER2 opens up new possibilities for positronium imaging in breast cancer diagnostics and treatment (Fig. 5).

B. Positronium imaging

During PET diagnosis of a living organism, annihilation of positrons proceeds via formation of positronium in as many as 40% of the cases (Harpen, 2004; Kotera, Saito, and Yamanaka, 2005; Jasinska *et al.*, 2017). This makes newly invented positronium imaging (Moskal *et al.*, 2021a) a promising method for the *in vivo* assessment of tissue pathology. Positronium imaging may be defined as a spatially resolved reconstruction of positronium properties in living organisms (Moskal, 2019). Information about positronium mean lifetime may be directly inferred by the application of $\beta^+\gamma$ emitters such as ^{44}Sc, which enable one to determine the positronium lifetime in the organism by measurement of the time of the emission of the prompt photon and the time of annihilation (Fig. 6). Coincident detection of both prompt and annihilation photons and registrations of their positions and times of interaction in the tomograph allows one to reconstruct the position of annihilation and lifetime of positronium in each image element (voxel) separately (on a voxel-by-voxel basis). For the reconstruction of the annihilation position and time, both 3γ self-annihilation of *o*-Ps (Gajos *et al.*, 2016; Moskal *et al.*, 2019, 2021b) and 2γ pickoff and conversion processes of *o*-Ps (Moskal *et al.*, 2020, 2021a) may be applied. A first multiphoton PET detector enabling positronium imaging was constructed based on plastic scinillators (Moskal *et al.*, 2014;

Niedzwiecki *et al.*, 2017; Dulski *et al.*, 2021). It recently provided *ex vivo* 2γ positronium images of phantoms (objects designed to test the imaging performance) built from cardiac myxoma cancer tissues and adipose tissues (Moskal *et al.*, 2021a), as well as 3γ images of the extended cylindrical phantoms (Moskal *et al.*, 2021b). Positronium mean lifetime imaging based on two photons is more than 300 times more effective than that based on three photons because (i) in the tissue, due to the pickoff and conversion processes, *o*-Ps decays about 70 times, viz., $\tau_0^o/\tau_{\text{tissue}} - 1$, more frequently to 2γ than to 3γ; (ii) the attenuation of 3γ events in the body is much larger (more than 4 times) with respect to 2γ, due to both the higher number of photons and their lower energies; and (iii) the efficiency for the detection and selection of 3γ is lower than for 2γ. The right panel of Fig. 6 shows a comparison of sensitivity for standard PET imaging and 2γ positronium imaging (Moskal and Stępień, 2020). The sensitivity for positronium imaging is lower since it requires registration of a prompt photon in addition to two annihilation photons. However, the sensitivity is increasing with the growth of the axial field of view, and the figure indicates that total-body PET systems (with a 200 cm long scanner) will provide even higher sensitivity for positronium imaging than current (20 cm long) scanners provide for standard PET diagnostics. Using the standard whole-body PET protocol, total-body PET sensitivity enables one to achieve determination of the positronium lifetime with the precision of about 20 ps for the $2 \times 2 \times 2$ cm^3 voxels (Moskal *et al.*, 2020, 2021a), and 2 ps when averaging over the entire organs (Moskal and Stępień, 2021); see Sec. VI.C. The time resolution for determining the mean *o*-Ps lifetime in the tissue depends
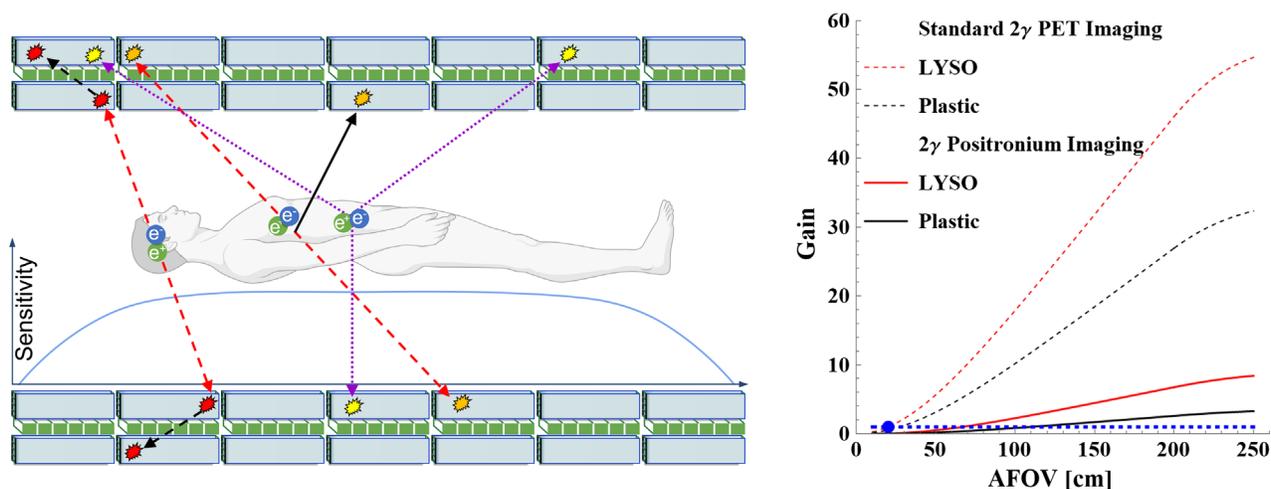
FIG. 6.   Left image: scheme of the example of total-body PET for the positronium and quantum entanglement imaging showing an axial cross section of the tomograph design composed of two detection layers. The single detection module consists of a scintillator and wavelength-shifting strips read out by silicon photomultiplier matrices. Here elements are not presented to scale. Dashed red arrows indicate example lines of response originating from e^+e^- annihilation. 2γ originating from the brain scatter twice in the plastic scintillator and are shown as an example of an event usable for quantum entanglement tomography discussed in Sec. VI.D. Violet dotted arrows indicate 3γ decay, and dashed red arrows together with solid black arrow indicate annihilation and the prompt photon useful for positronium imaging discussed in Sec. VI.B. Superimposed charts indicate the sensitivity (in arbitrary units) along the axial field of view (AFOV). Right panel: sensitivity for the 2γ positronium imaging (2 times annihilation γ plus a prompt photon) compared to the sensitivity for the standard 2γ PET imaging. Results for lutetium-yttrium oxyorthosilicate crystal (LYSO) PET and plastic PET are shown as a function of the scanner's AFOV. The sensitivity gain is shown with respect to the 20 cm AFOV LYSO PET (indicated with a horizontal blue dotted line). From Moskal and Stępień, 2020.

predominantly on the value of the mean *o*-Ps lifetime and may be estimated as $\tau_{\text{tissue}}/\sqrt{N}$, where N denotes the number of events in a given voxel of the positronium image (Moskal *et al.*, 2020). Assuming that $\tau_{\text{tissue}} = 2$ ns, it can be estimated that with 10^4 registered events per cm^3 [as expected for the total-body PET systems (Moskal *et al.*, 2020)], a resolution of $\sigma \approx 20$ ps is achievable. Interpretation of positronium properties as a diagnostic parameter will still require systematic research. The resolution of 20 ps obtained in the first *in vitro* images (Moskal *et al.*, 2021a) and expected for total-body PET systems (Moskal *et al.*, 2020) is sufficient to distinguish between the healthy and cancer tissues for which differences larger than 50 ps [in the range of 50–200 ps (Jasinska *et al.*, 2017; Zgardzinska *et al.*, 2020)] or even 700 ps (Moskal *et al.*, 2021a, 2023) are observed. Recently both the new methods for a precise analysis and decomposition of positron annihilation lifetime spectra (Dulski, 2020; Shibuya *et al.*, 2022) and new positronium image reconstruction methods were developed using maximum likelihood image estimation, with the latter resulting in spatial resolution of the image that is better than 4 mm (Qi and Huang, 2022; Zhu, Harrison, and Kao, 2022).

These results indicate that positronium imaging may be introduced in clinics for the assessment of tissue alterations at the molecular level before they lead to the functional and morphological changes (Moskal and Stępień, 2022). The practical diagnostic benefits of positronium imaging will be the subject of long-standing research and are yet to be determined. Here we hypothesized that when applied to brain diagnostics positronium imaging with its potential for the *in vivo* assessment of the changes of the nanostructure of tissues may become an early diagnostics indicator for neurodegenerative diseases such as dementia, Alzheimer's disease, and Parkinson's disease.

C. Positronium as a biomarker of hypoxia

The decay rate of orthopositronium in tissue due to the conversion processes on paramagnetic molecules is linearly proportional to the concentration on these molecules; see the discussion in Sec. III.D.2. Therefore, positronium may be used for an oxygen concentration assessment in tissue (Shibuya *et al.*, 2020; Stepanov *et al.*, 2020; Moskal and Stępień, 2021; Zare *et al.*, 2022). In this section the possibility of *in vivo* sensing of oxygen concentration by means of positronium mean lifetime determination is considered.

A normal level of oxygen concentration in the cells is referred to as normoxia, while hypoxia is defined as a state or condition in which oxygen supply is not sufficient to support physiological processes in tissues and organs. Local hypoxia is usually a result of vessels occlusion (arteries or arterioles) to cause stroke, myocardial infarction, or other organ injury leading to cell death, namely, necrosis (McKeown, 2014). In solid tumors hypoxia is often observed and leads to the development of an aggressive phenotype, acquired treatment resistance, and is associated with a poor prognosis (Brahimi-Horn, Chiche, and Pouyssegur, 2007; McKeown, 2014; Królicki and Kunikowska, 2021; Vaupel, Flood, and Swartz, 2021). Therefore, an *in vivo* assessment of the degree of hypoxia would be advantageous for personalized cancer therapy (Cramer and Vaupel, 2022). Recently it was argued

Tissue type			
1 – Myocardium	2 – Brain	3 – Kidney	4 – Liver
5 – Head and Neck	6 – Lung	7 – Prostate	8 – Skin melanoma
9 – Sarcoma	10 – Cervical	11 – Breast	12 - Pancreatic
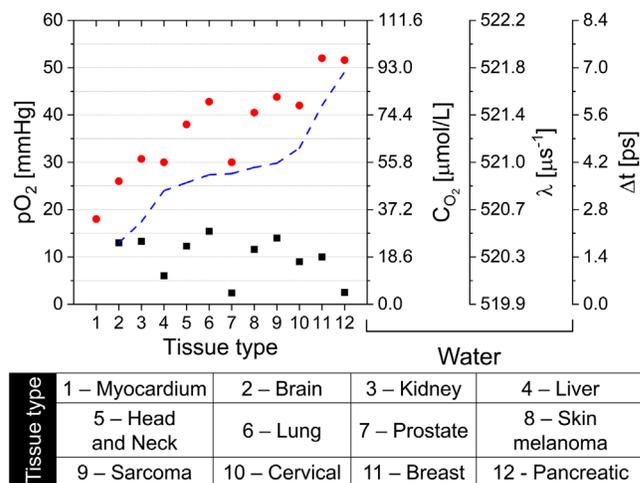
FIG. 7. Comparison of partial pressure of oxygen molecules (pO$_2$) in healthy and cancer tissues. The horizontal axis indicates a tissue type (1–12) explained beneath the graph. The right axes refer to water and indicate the concentration of oxygen (C_{O_2}), the *o*-Ps annihilation rate λ^o in water, and the change of the *o*-Ps mean lifetime Δt due to the concentration of oxygen molecules dissolved in water. Normal pO$_2$ for healthy tissues (red circles) and hypoxia in cancer tissues (black squares) are shown based on experimental data summarized and reviewed in medians that do not show real patient variability (Vaupel, Hockel, and Maye, 2007; McKeown, 2014; Swartz *et al.*, 2020; Vaupel, Flood, and Swartz, 2021). For head and neck tumors, sarcoma and normal subcutaneous tissue data were compiled from the studies by Nordsmark, Bentzen, and Overgaard (1994) and Becker *et al.* (1998). For a kidney and melanoma there were separate studies (Lartigau *et al.*, 1997; Lawrentschuk *et al.*, 2005). The tissue type is numbered according to the increasing partial pressure difference between healthy and cancerous tissue, which is indicated by the blue dashed line.

that the possibility of applying positronium imaging with total-body PET scanners opens perspectives for the application of positronium as a biomarker for an *in vivo* assessment of the degree of hypoxia (Moskal and Stępień, 2021). Figure 7 demonstrates that the partial pressure of oxygen (pO$_2$) in cancer tissues is significantly lower than in corresponding healthy tissue. The differences vary between 10 (for the brain) and 50 mmHg (for the pancreas).

The experimentally established relationship (for water) between the partial oxygen pressure pO$_2$ and the *o*-Ps decay rate constant λ^o reads (Shibuya *et al.*, 2020) pO$_2$[mmHg] $= 26.3(11) \times [\lambda^o - 519.9(16) \ \mu\text{s}^{-1}]$, where 519.9 μs^{-1} accounts for *o*-Ps self-annihilation and the pickoff rate in water. This relation indicates (as shown in Fig. 7) that the differences of pO$_2$ in the range of 10–50 mmHg result in the change of orthopositronium mean lifetime in water by about 2–7 ps. Estimation for water is the most pessimistic since for organic liquids (such as cyclohexane, isooctane, and isopropanol) these mean that *o*-Ps lifetime changes are larger (Shibuya *et al.*, 2020; Stepanov *et al.*, 2020; Stepanov, Byakova, and Stepanov, 2021). These estimations indicate that, in order to apply positronium as a biomarker for hypoxia, an extremaly high (few picosecond) mean lifetime resolution determination is required. A resolution of 20 ps was already obtained in the

first experimental positronium images for *ex vivo* studies of cardiac myxoma tumors (Moskal *et al.*, 2021a, 2023), with about 10^4 registered *o*-Ps annihilations. With 100 times more registered *o*-Ps annihilations (10^6), 2 ps resolution would be achievable. This number of annihilations can be collected by means of the total-body PET system for organs with a volume larger than 100 cm^3 (such as the pancreas or liver). Therefore, identification of hypoxia (organ averaged) using positronium as a biomarker may become feasible with total-body PET systems.

D. Quantum entanglement tomography

Photons originating from the decay of positronium are expected to be quantum entangled in polarization and exhibit nonlocal correlations, as discussed in Sec. IV.C. These correlations may be used for the improvement of the quality of PET image reconstruction (McNamara *et al.*, 2014; Toghyani *et al.*, 2016), and for the elaboration of new quantum biomarkers using entanglement witnesses as a diagnostic indicators (Hiesmayr and Moskal, 2017, 2019). The latter may work provided that the type and degree of quantum entanglement of photons from the decay of positronium is affected by the molecular environment in cells. This is a topic of current investigation (Hiesmayr and Moskal, 2017; Caradonna *et al.*, 2019; Sharma, Kumar, and Moskal, 2022) requiring new experimental input.

Figure 8 compares the distribution of the angle φ between scattering planes calculated under the assumption that photons from the *p*-Ps $\rightarrow 2\gamma$ process are entangled (black solid curve), for the case in which the scattering of one photon is completely independent of the scattering of the other photon (blue dashed curve), and for the case when photons originate from different annihilation processes (red dotted curve). Recently it was experimentally shown by Moskal (2018), Watts *et al.* (2021), and Abdurashitov *et al.* (2022) that the φ distribution for 2γ annihilations is indeed enhanced at $\varphi = 90°$, as expected for the quantum entangled state of 2γ.
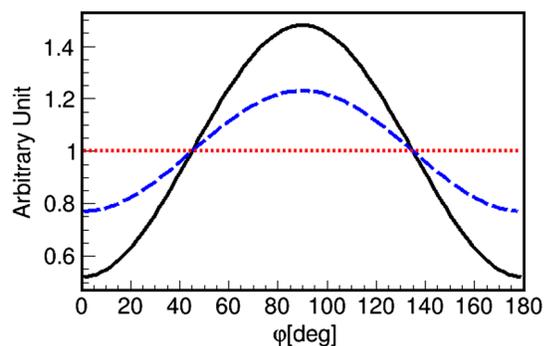
FIG. 8. Distribution of the angle φ between scattering planes of the photons emitted in *p*-Ps $\rightarrow 2\gamma$ when the photons are each scattered at $\theta \sim 82°$. For definitions of these angles see Fig. 4. The black solid curve corresponds to the photon pair being entangled, the dashed blue curve relates to independent Compton interaction of the two photons, and the red dotted line indicates when the photon polarizations are uncorrelated, as when the photons originate from two different *p*-Ps decays.

The image quality of standard 2γ PET may be improved by reduction of the fraction of events for which any of the photons was scattered in the patient, or for which photons originate from different annihilation events. This may be achieved by selecting events for which the angle between polarization direction of the two photons is close to $\varphi = 90°$ (McNamara *et al.*, 2014; Toghyani *et al.*, 2016; Moskal *et al.*, 2018; Watts *et al.*, 2021). Application of the selection based on the relative angle between the scattering planes will decrease the fraction of unwanted scatter and random events (Toghyani *et al.*, 2016) relative to the fraction of useful events. This will challenge the designs of PET systems, especially since the visibility of the quantum correlation is maximal for scattering angles around $\theta_1 = \theta_2 \sim 82°$, while the scattering cross section is the highest for forward scattered photons ($\theta_1 = \theta_2 \sim 0°$) (Klein and Nishina, 1929).

E. Road map for multiphoton total-body positron and positronium tomography

Positron emission tomography is presently experiencing a quantitative change in the diagnosis paradigm (Moskal and Stępień, 2020; Surti, Pantel, and Karp, 2020; Vanderberghe, Moskal, and Karp, 2020; Alavi *et al.*, 2021; Królicki and Kunikowska, 2021; Djekidel *et al.*, 2022). With the advent of total-body PET systems (Niedzwiecki *et al.*, 2017; Badawi *et al.*, 2019; Karp *et al.*, 2020; Hu *et al.*, 2022; Prenosil *et al.*, 2022) covering the entire human body (with a detector length of about 2 m), the simultaneous imaging of the metabolism rate of all organs and tissues in the body becomes possible. This opens possibilities for studies in physiology, biochemistry, and pharmacology of the kinetics of administered pharmaceuticals in the entire body, and in determining pharmaceuticals' uptake correlations in close and distant organs (Badawi *et al.*, 2019; Zhang *et al.*, 2020). High sensitivity of total-body PET systems (Surti, Pantel, and Karp, 2020; Vanderberghe, Moskal, and Karp, 2020) (up to a factor of ~40 higher with respect to standard 20 cm long PET; see Fig. 6) also enables dynamic- and kinetic-model-based parametric imaging (Feng *et al.*, 2021; Wang *et al.*, 2022), and therefore increases the diagnosis specificity in differentiating between healthy and cancerous tissues. In parallel, recent development in PET technology resulted in the first multiphoton (multigamma) PET system (Moskal *et al.*, 2021b) capable of positronium imaging (Moskal *et al.*, 2021a) based on the registration of two (Moskal *et al.*, 2020) or three photons (Moskal *et al.*, 2019) from positronium annihilations and the prompt photon from deexcitation of isotopes attached to pharamaceuticals. Moreover, there is a continual development of new materials (Lecoq, 2022; Lecoq *et al.*, 2022) and new systems and techniques (Cates and Levin, 2019; Gundacker *et al.*, 2019; Ota *et al.*, 2019; Kwon *et al.*, 2021; Tao *et al.*, 2021; Jensen *et al.*, 2022) for improving time and spatial resolution to the point where imaging by direct determination of the density distribution of annihilation points will become possible. The direct PET image of a 2D brain phantom was experimentally demonstrated with a spatial resolution of 4.8 mm (Kwon *et al.*, 2021). The new generation of total-body PET systems will combine high sensitivity with multiphoton imaging, and then

also with high timing resolution. The technology for the multiphoton total-body imaging is known, and it is at the stage of translation into clinics (Moskal and Stępień, 2022). The annihilation photons' detection technology for PET is also developing toward a more cost-effective solution focusing on plastic scintillators (Moskal and Stępień, 2020) and sparse detector configurations (Karakatsanis *et al.*, 2022). We stress that total-body multiphoton PET systems will also enable high precision studies of fundamental positronium decays (Moskal *et al.*, 2016) by increasing efficiency for the studies of three-photon positronium decays by more than an order of magnitude compared to present detectors (Moskal *et al.*, 2021b).

VII. CONCLUSIONS AND PERSPECTIVES

Positronium, the bound state of e^-e^+, is interesting both in fundamental physics and in applications ranging from anti-matter research to biology and medicine. The properties of positronium formation and decay in medium depend on the chemical environment and open new windows of opportunity in the biological and medical sciences. Effective mean decay rates are sensitive to the health of biological tissue, with interesting prospects to revolutionize next generation total-body PET scanning through positronium imaging as a new tool for medical diagnosis.

Traditional PET is based on the parameters of the concentration of the radiopharmaceutical and does not take into account changes in the positronium annihilation mechanism due to the chemical environment. The average lifetime of positronium, due to its sensitivity to changes in the nano-structure, allows us to take into account an additional parameter in the reconstruction of the histopathological image.

In this Colloquium we have surveyed prime topics in positronium physics and new prospects for medical applications. We conclude with a summary of key issues and open questions where next generation experiments should yield vital information:

- When one pushes the limits of QED bound state theory, anomalies between data in spectroscopic measurements and theory call for new precision measurements of positronium. Are there missed systematics, or might the data be pointing to new (bound state) physics waiting to be understood?
- Studies of gravity on antimatter will provide new tests of the equivalence principle. Does gravity couple equally to matter as to antimatter?
- Might next generation experiments searching for invisible decays of positronium help in the understanding of dark matter?
- About 40% of the positrons in conventional PET scans are formed via positronium intermediate states. Can this be developed through positronium imaging as a practical tool for medical diagnostics? Might imaging diagnostics be further enhanced by sensing the quantum entanglement of emitted photons?
- Traditional histopathological imaging requires punctual tissue sampling, which is always somewhat invasive for the patient. More traditional liquid biopsies, which are based on taking a sample of blood or other body fluid, does not give the possibility of locating the lesion. Might virtual biopsy with positronium imaging be able to tell us whether or not the tissue is cancerous without the need for invasive incision?
- Possible differences expected in mean *o*-Ps lifetime between healthy and cancerous tissues are due predominantly to the structural changes caused by the increased overexpression of receptors, cell-cycle controlling molecules, and other changes in metabolic pathways (due to inherited or acquired mutations), and to some extent by the changes of the concentration of the molecular oxygen dissolved in cells. The influence of the oxygen concentration on the mean *o*-Ps lifetime may enable an organ-averaged identification of hypoxia with positronium as a biomarker. How might this be translated to clinics?

REFERENCES

Abdurashitov, D., *et al.*, 2022, J. Instrum. **17**, P03010.

Acin, A., J. I. Latorre, and P. Pascual, 2001, Phys. Rev. A **63**, 042107.

Adkins, G. S., D. B. Cassidy, and J. Pérez-Ríos, 2022, Phys. Rep. **975**, 1.

Adkins, G. S., R. N. Fell, and P. M. Mitrikov, 1997, Phys. Rev. Lett. **79**, 3383.

Adkins, G. S., R. N. Fell, and J. Sapirstein, 2002, Ann. Phys. (Amsterdam) **295**, 136.

Adkins, G. S., N. M. McGovern, R. N. Fell, and J. Sapirstein, 2003, Phys. Rev. A **68**, 032512.

Aghion, S., *et al.* (AEgIS Collaboration), 2016, Phys. Rev. A **94**, 012507.

Aghion, S., *et al.* (AEgIS Collaboration), 2018, Phys. Rev. A **98**, 013402.

Akiyama, Y., Y. Shibahara, S. Takeda, Y. Izumi, Y. Honda, S. Tagawa, and S. Nishijima, 2007, J. Polym. Sci. B **45**, 2031.

Alavi, A., and M. Reivich, 2002, Semin. Nucl. Med. **32**, 2.

Alavi, A., T. J. Werner, E. Ł. Stępień, and P. Moskal, 2021, Bio-Algorithms Med-Syst. **17**, 203.

Al-Ramadhan, A. H., and D. W. Gidley, 1994, Phys. Rev. Lett. **72**, 1632.

Amsler, C., *et al.* (AEgIS Collaboration), 2019, Phys. Rev. A **99**, 033405.

Amsler, C., *et al.* (AEgIS Collaboration), 2021, Commun. Phys. **4**, 19.

Andersen, S. L., D. B. Cassidy, J. Chevallieri, B. S. Cooper, A. Deller, T. E. Wall, and U. I. Uggerhoj, 2015, J. Phys. B **48**, 204003.

Anderson, C. D., 1933, Phys. Rev. **43**, 491.

Andreev, V., *et al.* (ACME Collaboration), 2018, Nature (London) **562**, 355.

Aoyama, T., T. Kinoshita, and M. Nio, 2018, Phys. Rev. D **97**, 036001.

Avachat, A. V., A. G. Leja, K. H. Mahmoud, M. A. Anastasio, M. Sivaguru, and A. Di Fulvio, 2022, 10.21203/rs.3.rs-1657111/v1.

Avetissian, H. K., A. K. Avetissian, and G. F. Mkrtchian, 2014, Phys. Rev. Lett. **113**, 023904.

Avril, N., 2004, J. Nucl. Med. **45**, 930, https://jnm.snmjournals.org/content/jnumed/45/6/930.full.pdf.

Axpe, E., A. B. García-Arribas, J. I. Mujika, D. Mérida, A. Alonso, X. Lopez, J. A. García, J. M. Ugalde, F. M. Goñi, and F. Plazaola, 2015, RSC Adv. **5**, 44282.

Axpe, E., T. Lopez-Euba, A. Castellanos-Rubio, D. Merida, J. A. Garcia, L. Plaza-Izurieta, N. Fernandez-Jimenez, F. Plazaola, and J. R. Bilbao, 2014, PLoS One **9**, e83838.

Badawi, R. D., *et al.*, 2019, J. Nucl. Med. **60**, 299.

Bass, S. D., 2019, Acta Phys. Pol. B **50**, 1319.

Becker, A., G. Hansgen, M. Bloching, C. Weigel, C. Lautenschlager, and J. Dunst, 1998, Int. J. Radiat. Oncol. Biol. Phys. **42**, 35.

Berko, S., and H. N. Pendleton, 1980, Annu. Rev. Nucl. Part. Sci. **30**, 543.

Bernreuther, W., U. Low, J. P. Ma, and O. Nachtmann, 1988, Z. Phys. C **41**, 143.

Blanco, F., A. Muñoz, D. Almeida, F. Ferreira da Silva, P. Limão-Vieira, M. C. Fuss, A. G. Sanz, and G. García, 2013, Eur. Phys. J. D **67**, 199.

Blanco, F., *et al.*, 2016, J. Phys. B **49**, 145001.

Brahimi-Horn, C. M., J. Chiche, and J. Pouyssegur, 2007, J. Mol. Med. (Cham, Switz.) **85**, 1301.

Brandt, W., S. Berko, and W. W. Walker, 1960, Phys. Rev. **120**, 1289.

Brandt, W., and J. Wilkenfeld, 1975, Phys. Rev. B **12**, 2579.

Brown, B. J., 1974, Aust. J. Chem. **27**, 1125.

Bura, Z., K. Dulski, E. Kubicz, P. Malczak, M. Pędziwiatr, M. Szczepanek, E. Ł. Stępień, and P. Moskal, 2020, Acta Phys. Pol. B **51**, 377.

Caradonna, P., D. Reutens, T. Takahashi, S. Takeda, and V. Vegh, 2019, J. Phys. Commun. **3**, 105005.

Cassidy, D. B., 2018, Eur. Phys. J. D **72**, 53.

Cassidy, D. B., P. Crivelli, T. H. Hisakado, L. Liszkay, V. E. Meligne, P. Perez, H. W. K. Tom, and A. P. Mills, 2010, Phys. Rev. A **81**, 012715.

Cassidy, D. B., S. H. M. Deng, and R. G. Greaves, 2006, Rev. Sci. Instrum. **77**, 073106.

Cassidy, D. B., T. H. Hisakado, H. W. K. Tom, and A. P. Mills, 2012, Phys. Rev. Lett. **108**, 043401.

Cassidy, D. B., and A. P. Mills, 2007, Nature (London) **449**, 195.

Cassidy, D. B., K. T. Yokoyama, S. H. M. Deng, D. L. Griscom, H. Miyadera, H. W. K. Tom, C. M. Varma, and A. P. Mills, 2007, Phys. Rev. B **75**, 085415.

Caswell, W. E., and G. P. Lepage, 1986, Phys. Lett. **167B**, 437.

Cates, J. W., and C. S. Levin, 2019, Phys. Med. Biol. **64**, 175016.

Cegła, P., and T. Piotrowski, 2021, Bio-Algorithms Med-Syst. **17**, 259.

Chamerski, K., W. Korzekwa, J. Filipecki, O. Shpotyuk, M. Stopa, P. Jelen, and M. Sitarz, 2017, Nanoscale Res. Lett. **12**, 303.

Champion, Ch., 2005, Braz. Arch. Biol. Technol. **48**, 191.

Chang, T., M. Xu, and X. Zeng, 1987, Phys. Lett. A **126**, 189.

Charlton, M., *et al.* (GBAR Collaboration), 2021, Nucl. Instrum. Methods Phys. Res., Sect. A **985**, 164657.

Chen, H., J. D. van Horn, and Y. C. Jean, 2012, Defect Diffus. Forum **331**, 275.

Choiński, J., and M. Łyczko, 2021, Bio-Algorithms Med-Syst. **17**, 241.

Chow, E. I. H., S. Y. Chuang, and P. K. Tseng, 1981, Biochim. Biophys. Acta Biomembr. **646**, 356.

Čížek, J., M. Vlček, and P. Procházka, 2012, New J. Phys. **14**, 035005.

Coleman, P. G., 2003, in *Principles and Applications of Positron and Positronium Chemistry*, edited by Y. C. Jean, P. E. Mellon, and D. M. Schrader (World Scientific, Singapore).

Consolati, G., R. Ferragut, A. Galarneau, F. Di Renzo, and F. Quasso, 2013, Chem. Soc. Rev. **42**, 3821.

Conti, M., 2009, Phys. Med. **25**, 1.

Cooper, B. S., A. M. Alonso, A. Deller, L. Liszkay, and D. B. Cassidy, 2016, Phys. Rev. B **93**, 125305.

Cramer, T., and P. Vaupel, 2022, J. Hepatol. **76**, 975.

Crivelli, P., U. Gendotti, A. Rubbia, L. Liszkay, P. Perez, and C. Corbel, 2010, Phys. Rev. A **81**, 052703.

Czarnecki, A., K. Melnikov, and A. Yelkhovsky, 1999, Phys. Rev. Lett. **82**, 311.

Danielson, J. R., D. H. E. Dubin, R. G. Greaves, and C. M. Surko, 2015, Rev. Mod. Phys. **87**, 247.

Dauwe, C., B. van Waeyenberge, and J. de Baerdemaeker, 2005, Acta Phys. Pol. A **107**, 623.

Deutsch, M., 1951, Phys. Rev. **82**, 455.

Dirac, P. A. M., 1931, Proc. R. Soc. A **133**, 60.

Djekidel, M., R. AlSadi, M. Abi Akl, S. Vandenberghe, and O. Bouhali, 2022, Eur. J. Nucl. Med. Mol. Imaging **49**, 3624.

Dlubek, G., H. M. Fretwell, and M. A. Alam, 2000, Macromolecules **33**, 187.

Doser, M., *et al.*, 2018, Phil. Trans. R. Soc. A **376**, 20170274.

Dryzek, J., T. Suzuki, and R. Yu, 2007, Radiat. Phys. Chem. **76**, 297.

Dufour, G., D. B. Cassidy, P. Crivelli, P. Debu, A. Lambrecht, V. V. Nesvizhevsky, S. Reynaud, A. Y. Voronin, and T. E. Wall, **2015**, Adv. High Energy Phys. 379642.

Dulski, K., 2020, Acta Phys. Pol. A **137**, 167.

Dulski, K., *et al.*, 2021, Nucl. Instrum. Methods Phys. Res., Sect. A **1008**, 165452.

Dupasquier, A., P. De Natale, and A. Rolando, 1991, Phys. Rev. B **43**, 10036.

Dupasquier, A., and A. Zecca, 1985, Riv. Nuovo Cimento **8**, 1.

Eldrup, M., and O. Mogensen, 1972, J. Chem. Phys. **57**, 495.

Eldrup, M., A. Vehanen, Peter J. Schultz, and K. G. Lynn, 1983, Phys. Rev. Lett. **51**, 2007.

Eldrup, M., A. Vehanen, Peter J. Schultz, and K. G. Lynn, 1985, Phys. Rev. B **32**, 7048.

Elias, M. M., A. H. Al-Mashhadani, and Z. T. Al-Shiebani, 2001, Dirasat Pure Sci. **28**, 240, https://applications.emro.who.int/imemrf/80/Dirasat-2001-28-2-240-244-eng.pdf.

Feng, I. J., R. H. Pratt, and H. K. Tseng, 1981, Phys. Rev. A **24**, 1358.

Feng, T., Y. Zhao, H. Shi, H. Li, X. Zhang, G. Wang, P. M. Price, R. D. Badawi, S. R. Cherry, and T. Jones, 2021, J. Nucl. Med. **62**, 738.

Ferrell, R. A., 1958, Phys. Rev. **110**, 1355.

Filosofov, D. V., *et al.*, 2010, Radiochim. Acta **98**, 149.

Gajos, A., *et al.*, 2016, Nucl. Instrum. Methods Phys. Res., Sect. A **819**, 54.

García-Arribas, A. B., *et al.*, 2016, Langmuir **32**, 5434.

Gninenko, S. N., N. V. Krasnikov, and A. Rubbia, 2002, Mod. Phys. Lett. A **17**, 1713.

Goworek, T., 2014, Ann. Univ. Mariae Curie-Skłodowska, Sect. AA **LXIX**, 1.

Gregory, R. B., K. J. Chai, and W. Su, 1992, Mater. Sci. Forum **105–110**, 1577.

Gullikson, E. M., and A. P. Mills, 1986, Phys. Rev. Lett. **57**, 376.

Gundacker, S., R. Martinez Turtos, E. Auffray, M. Paganoni, and P. Lecoq, 2019, Phys. Med. Biol. **64**, 055012.

Gurung, L., T. J. Babij, S. D. Hogan, and D. B. Cassidy, 2020, Phys. Rev. Lett. **125**, 073002.

Gurung, L., T. J. Babij, J. Pérez-Ríos, S. D. Hogan, and D. B. Cassidy, 2021, Phys. Rev. A **103**, 042805.

Gustafson, D. R., 1970, Biophys. J. **10**, 316.

Handel, E. D., G. Graf, and J. C. Glass, 1976, J. Am. Chem. Soc. **98**, 2360.

Handel, E. D., G. Graf, and J. C. Glass, 1980, Biophys. J. **32**, 697.

Hanneke, D., S. Fogwell, and G. Gabrielse, 2008, Phys. Rev. Lett. **100**, 120801.

Hansen, E. H., and U. Ingerslev-Jensen, 1983, J. Phys. D **16**, 1353.

Harpen, M. D., 2004, Med. Phys. **31**, 57.

Hatcher, C. R., W. E. Millett, and L. Brown, 1958, Phys. Rev. **111**, 12.

Hawari, A. I., D. W. Gidley, J. Moxom, A. G. Hathaway, and S. Mukherjee, 2011, J. Phys. Conf. Ser. **262**, 012024.

He, C., T. Ohdaira, N. Oshima, M. Muramatsu, A. Kinomura, R. Suzuki, T. Oka, and Y. Kobayashi, 2007, Phys. Rev. B **75**, 195404.

Heiss, M., G. Wichmann, A. Rubbia, and P. Crivelli, 2018, J. Phys. Conf. Ser. **1138**, 012007.

Henry, K. E., G. A. Ulaner, and J. S. Lewis, 2018, PET Clin. **13**, 423.

Hernandez, R., H. F. Valdovinos, Y. Yang, R. Chakravarty, H. Hong, T. E. Barnhart, and W. Cai, 2014, Mol. Pharmaceutics **11**, 2954.

Hiesmayr, B. C., and P. Moskal, 2017, Sci. Rep. **7**, 15349.

Hiesmayr, B. C., and P. Moskal, 2019, Sci. Rep. **9**, 8166.

Hoang, A. H., P. Labelle, and S. M. Zebarjad, 1997, Phys. Rev. Lett. **79**, 3387.

Howell, R. H., R. A. Alvarez, and M. Stanek, 1982, Appl. Phys. Lett. **40**, 751.

Hu, H., *et al.*, 2022 (to be published),10.21203/rs.3.rs-1920965/v1.

Hugenschmidt, C., 2016, Surf. Sci. Rep. **71**, 547.

Hugenschmidt, C., B. Löwe, J. Mayer, C. Piochacz, P. Pikart, R. Repper, M. Stadlbauer, and K. Schreckenbach, 2008, Nucl. Instrum. Methods Phys. Res., Sect. A **593**, 616.

Humm, J. L., A. Rosenfeld, and A. Del Guerra, 2003, Eur. J. Nucl. Med. Mol. Imaging **30**, 1574.

Hunt, A. W., D. B. Cassidy, P. A. Sterne, T. E. Cowan, R. H. Howell, K. G. Lynn, and J. A. Golovchenko, 2001, Phys. Rev. Lett. **86**, 5612.

Ishida, A., T. Namba, S. Asai, T. Kobayashi, H. Saito, M. Yoshida, K. Tanaka, and A. Yamamoto, 2014, Phys. Lett. B **734**, 338.

Ishida, A., *et al.*, 2012, Hyperfine Interact. **212**, 133.

Ito, K., R. S. Yu, K. Sato, K. Hirata, and Y. Kobayashi, 2005, J. Appl. Phys. **98**, 094307.

Jasinska, B., *et al.*, 2016, Acta Phys. Pol. B **47**, 453.

Jasinska, B., *et al.*, 2017, Acta Phys. Pol. B **48**, 1737.

Jean, Y., P. E. Mallon, and D. M. Schrader, 2003, in *Principles and Applications of Positron and Positronium Chemistry*, edited by Y. C. Jean, P. E. Mellon, and D. M. Schrader (World Scientific, Singapore).

Jean, Y. C., and H. J. Ache, 1977, J. Am. Chem. Soc. **99**, 1623.

Jean, Y. C., H. Chen, G. Liu, and J. E. Gadzin, 2007, Radiat. Phys. Chem. **76**, 70.

Jean, Y. C., and A. J. Hancock, 1982, J. Chem. Phys. **77**, 5836.

Jean, Y. C., Y. Li, G. Liu, H. Chen, J. Zhang, and J. E. Gadzia, 2006, Appl. Surf. Sci. **252**, 3166.

Jensen, M. L., J. S. Nyemann, L. P. Muren, B. Julsgaard, P. Balling, and R. M. Turtos, 2022, Sci. Rep. **12**, 8301.

Kakimoto, M., T. Hyodo, T. Chiba, T. Akahane, and T. B. Chang, 1987, J. Phys. B **20**, L107.

Kamińska, D., *et al.*, 2016, Eur. Phys. J. C **76**, 445.

Karakatsanis, N. A., M. H. Nehmeh, M. Conti, G. Bal, A. J. González, and S. A. Nehmeh, 2022, Phys. Med. Biol. **67**, 105010.

Karimi, H., B. Leszczynski, T. Kolodziej, E. Kubicz, M. Przybylo, and E. Stępień, 2020, Micron **137**, 102917.

Karp, J. S., V. Viswanath, M. J. Geagan, G. Muehllehner, A. R. Pantel, A. E. Parma, M. J. Perkins, J. P. Schmall, M. E. Werner, and M. E. Daube-Witherspoon, 2020, J. Nucl. Med. **61**, 136.

Karshenboim, S. G., 2004, Int. J. Mod. Phys. A **19**, 3879.

Karshenboim, S. G., 2005, Phys. Rep. **422**, 1.

Kataoka, Y., S. Asai, and T. Kobayashi, 2009, Phys. Lett. B **671**, 219.

Kerr, D. P., and B. G. Hogg, 1962, J. Chem. Phys. **36**, 2190.

Kilburn, D., S. Townrow, V. Meunier, R. Richardson, A. Alam, and J. Ubbink, 2006, Nat. Mater. **5**, 632.

Kim, L., R. H. Pratt, S. M. Seltzer, and M. J. Berger, 1986, Phys. Rev. A **33**, 3002.

Kinoshita, T., and G. P. Lepage, 1990, Adv. Ser. Dir. High Energy Phys. **7**, 81.

Klein, O. J., and Y. Nishina, 1929, Z. Phys. **52**, 853.

Kotera, K., T. Saito, and T. Yamanaka, 2005, Phys. Lett. A **345**, 184.

Krasnicky, D., R. Caravita, C. Canali, and G. Testera, 2016, Phys. Rev. A **94**, 022714.

Królicki, L., and J. Kunikowska, 2021, Bio-Algorithms Med-Syst. **17**, 213.

Kubica, P., and A. T. Stewart, 1975, Phys. Rev. Lett. **34**, 852.

Kubicz, E., *et al.*, 2015, Nukleonika **60**, 749.

Kuhl, D. E., and R. Q. Edwards, 1963, Radiology **80**, 653.

Kwon, S. I., R. Ota, E. Berg, F. Hashimoto, K. Nakajima, I. Ogawa, Y. Tamagawa, T. Omura, T. Hasegawa, and S. R. Cherry, 2021, Nat. Photonics **15**, 914.

Labelle, P., 1992, arXiv:hep-ph/9209266.

Lartigau, E., H. Randrianarivelo, M. F. Avril, A. Margulis, A. Spatz, F. Eschwège, and M. Guichard, 1997, Mel. Res. **7**, 400.

Lawrentschuk, N., A. M. Poon, S. S. Foo, L. G. Putra, C. Murone, I. D. Davis, D. M. Bolton, and A. M. Scott, 2005, Int. Braz. J. Urol. **96**, 540.

Lecoq, P., 2022, Eur. Phys. J. Plus **137**, 964.

Lecoq, P., G. Konstantinou, R. Latella, L. Moliner, J. Nuyts, L. Zhang, J. Barrio, J. M. Benlloch, and A. J. Gonzalez, 2022, IEEE Trans. Radiat. Plasma Med. Sci. **6**, 510.

Lin, E. C., and A. Alavi, 2019, *PET and PET/CT: A Clinical Guide*, 3rd ed. (Thieme Medical Publishers, New York), p. 3.

Liszkay, L., *et al.*, 2012, New J. Phys. **14**, 065009.

Liu, G., H. Chen, L. Chakka, M.-L. Cheng, J. E. Gadzia, R. Suzuki, T. Ohdaira, N. Oshima, and Y. C. Jean, 2008, Appl. Surf. Sci. **255**, 115.

Liu, G., H. Chen, L. Chakka, J. E. Gadzia, and Y. C. Jean, 2007, Phys. Status Solidi C **4**, 3912.

Lynn, K. G., and D. O. Welch, 1980, Phys. Rev. B **22**, 99.

Mariazzi, S., P. Bettotti, and R. S. Brusa, 2010, Phys. Rev. Lett. **104**, 243401.

Mariazzi, S., P. Bettotti, S. Larcheri, L. Toniutti, and R. S. Brusa, 2010, Phys. Rev. B **81**, 235418.

Mariazzi, S., R. Caravita, M. Doser, G. Nebbia, and R. S. Brusa, 2020, Eur. Phys. J. D **74**, 79.

Mariazzi, S., B. Rieneacker, R. Magrin Maffei, L. Povolo, S. Sharma, R. Caravita, L. Penasa, P. Bettotti, M. Doser, and R. S. Brusa, 2022, Phys. Rev. B **105**, 115422.

Mariazzi, S., A. Salemi, and R. S. Brusa, 2008, Phys. Rev. B **78**, 085428.

Mariazzi, S., *et al.*, 2021, J. Phys. B **54**, 085004.

Marom, E. M., M. B. Aloia, T. A. Moore, M. Hara, J. E. Herndon II, D. H. Harpole, Jr., P. C. Goodman, and E. F. Patz, Jr., 2001, Lung Cancer **33**, 99.

Matulewicz, T., 2021, Bio-Algorithms Med-Syst. **17**, 235.

McKeown, S. R., 2014, Br. J. Radiol. **87**, 20130676.

McNamara, A. L., M. Toghyani, J. E. Gillam, K. Wu, and Z. Kuncic, 2014, Phys. Med. Biol. **59**, 7587.

Mikolajczyk, R., S. Huclier-Markai, C. Alliot, F. Haddad, D. Szikra, V. Forgacs, and P. Garnuszek, 2021, EJNMMI Radiopharm. Chem. **6**, 19.

Mills, A. P., 1983, Phys. Rev. A **27**, 262–267.

Mills, A. P., 2019, Phys. Rev. A **100**, 063615.

Mills, A. P., and E. M. Gullikson, 1986, Appl. Phys. Lett. **49**, 1121.

Mills, A. P., and M. Leventhal, 2002, Nucl. Instrum. Methods Phys. Res., Sect. B **192**, 102.

Mills, A. P., P. M. Platzman, and B. L. Brown, 1978, Phys. Rev. Lett. **41**, 1076.

Mills, Jr., A. P., S. S. Voris, Jr., and T. S. Andrew, 1994, J. Appl. Phys. **76**, 2556.

Miyazaki, A., T. Yamazaki, T. Suehara, T. Namba, S. Asai, T. Kobayashi, H. Saito, Y. Tatematsu, I. Ogawa, and T. Idehara, **2015**, Prog. Theor. Exp. Phys. 011C01.

Mogensen, O. E., 1974, J. Chem. Phys. **60**, 998.

Mohorovicic, S., 1934, Astron. Nachr. **253**, 93.

Morel, L., Z. Yao, P. Cladé, and S. Guellati-Khélifa, 2020, Nature (London) **588**, 61.

Moskal, P., 2018, in *Proceedings of the IEEE Nuclear Science Symposium and Medical Imaging Conference, Sydney, 2018* (IEEE, New York), p. 1, https://ieeexplore.ieee.org/document/8824622.

Moskal, P., 2019, in *Proceedings of the IEEE Nuclear Science Symposium and Medical Imaging Conference, Manchester, England, 2019* (IEEE, New York), p. 1, https://ieeexplore.ieee.org/document/9059856.

Moskal, P., B. Jasinska, E. Stępień, and S. D. Bass, 2019, Nat. Rev. Phys. **1**, 527.

Moskal, P., E. Kubicz, G. Grudzień, E. Czerwiński, K. Dulski, B. Leszczyński, S. Niedźwiecki, and E. Ł. Stępień, 2023, EJNMMI Phys. **10**, 22.

Moskal, P., and E. Ł. Stępień, 2020, PET Clin. **15**, 439.

Moskal, P., and E. Ł. Stępień, 2021, Bio-Algorithms Med-Syst. **17**, 311.

Moskal, P., and E. Ł. Stępień, 2022, Front. Phys. **10**, 969806.

Moskal, P., *et al.*, 2014, Nucl. Instrum. Methods Phys. Res., Sect. A **764**, 317.

Moskal, P., *et al.*, 2016, Acta Phys. Pol. B **47**, 509.

Moskal, P., *et al.*, 2018, Eur. Phys. J. C **78**, 970.

Moskal, P., *et al.*, 2019, Phys. Med. Biol. **64**, 055017.

Moskal, P., *et al.*, 2020, EJNMMI Phys. **7**, 44.

Moskal, P., *et al.*, 2021a, Sci. Adv. **7**, eabh4394.

Moskal, P., *et al.*, 2021b, Nat. Commun. **12**, 5658.

Murphy, T. J., and C. M. Surko, 1992, Phys. Rev. A **46**, 5696.

Nagashima, Y., 2014, Phys. Rep. **545**, 95.

Nagashima, Y., Y. Morinaka, T. Kurihara, Y. Nagai, T. Hyodo, T. Shidara, and K. Nakahara, 1998, Phys. Rev. B **58**, 12676.

Nagashima, Y., *et al.*, 1995, Phys. Rev. A **52**, 258.

Niedzwiecki, S., *et al.*, 2017, Acta Phys. Pol. B **48**, 1567.

Nielsen, B., K. G. Lynn, and Y. C. Chen, 1986, Phys. Rev. Lett. **57**, 1789.

Nieminen, R. M., and J. Oliva, 1980, Phys. Rev. B **22**, 2226.

Nordsmark, M., S. M. Bentzen, and J. Overgaard, 1994, Acta Oncol. **33**, 383.

Nowakowski, M., and D. Bedoya Fierro, 2017, Acta Phys. Pol. B **48**, 1955.

Oberthaler, M. K., 2002, Nucl. Instrum. Methods Phys. Res., Sect. B **192**, 129.

Ore, A., 1949, Univ. Bergen, Arbok, Naturvitensk. Rekke **9**.

Ota, R., K. Nakajima, I. Ogawa, Y. Tamagawa, H. Shimoi, M. Suyama, and T. Hasegawa, 2019, Phys. Med. Biol. **64**, 07LT01.

Pachucki, K., and S. G. Karshenboim, 1998, Phys. Rev. Lett. **80**, 2101.

Pages, L., E. Bertel, H. Joffre, and L. Sklavenitis, 1972, At. Data Nucl. Data Tables **4**, 1.

Pamula, E., and E. Dryzek, 2008, Acta Phys. Pol. A **113**, 1485..

Pamula, E., E. Dryzek, and P. Dobrzynski, 2006, Acta Phys. Pol. A **110**, 631.

Parker, R. H., C. Yu, W. Zhong, B. Estey, and H. Müller, 2018, Science **360**, 191.

Perez, P., and Y. Sacquin, 2012, Classical Quantum Gravity **29**, 184008.

Perkins, A., and J. P. Carbotte, 1970, Phys. Rev. B **1**, 101.

Pethrick, R. A., 1997, Prog. Polym. Sci. **22**, 1.

Platzman, P. M., and A. P. Mills, 1994, Phys. Rev. B **49**, 454.

Prenosil, G. A., H. Sari, M. Fürstner, A. Afshar-Oromieh, K. Shi, A. Rominger, and M. Hentschel, 2022, J. Nucl. Med. **63**, 476.

Pruszynski, M., N. S. Loktionova, D. V. Filosofov, and F. Rösch, 2010, Appl. Radiat. Isot. **68**, 1636.

Puska, M. J., and R. M. Nieminen, 1994, Rev. Mod. Phys. **66**, 841.

Qi, J., and B. Huang, 2022, IEEE Trans. Med. Imaging **41**, 2848.

Reivich, M., *et al.*, 1979, Circ. Res. **44**, 127.

Ritter, M. W., P. O. Egan, V. W. Hughes, and K. A. Woodle, 1984, Phys. Rev. A **30**, 1331.

Roesch, F., 2012, Curr. Radiopharm. **5**, 187.

Rosar, F., H. G. Buchholz, S. Michels, M. A. Hoffmann, M. Piel, C. M. Waldmann, F. Rösch, S. Reuss, and M. Schreckenberger, 2020, EJNMMI Phys. **7**, 16.

Rubin, I., and Y. Yarden, 2001, Ann. Oncol. **12**, S3.

Saito, H., and T. Hyodo, 1999, Phys. Rev. B **60**, 11070.

Sane, P., E. Salonen, E. Falck, J. Repakova, F. Tuomisto, J. M. Holopainen, and I. Vattulainen, 2009, J. Phys. Chem. B **113**, 1810.

Sane, P., F. Toumisto, and J. M. Holopainen, 2011, Contact Lens Anterior Eye **34**, 2.

Sane, P., F. Tuomisto, S. K. Wiedmer, T. Nyman, I. Vattulainen, and J. M. Holopainen, 2010, Biochim. Biophys. Acta **1798**, 958.

Sato, K., *et al.*, 2015, Nucl. Instrum. Methods Phys. Res., Sect. B **342**, 104.

Sawyers, C. L., 2019, Cell **179**, 8.

Schultz, P. J., and J. L. Campbell, 1985, Phys. Lett. **112A**, 316.

Schultz, P. J., and K. G. Lynn, 1988, Rev. Mod. Phys. **60**, 701.

Schut, H., A. van Veen, J. de Roode, and F. Labohm, 2004, Mater. Sci. Forum **445**–**446**, 507.

Sferlazzo, P., S. Berko, and K. F. Canter, 1985, Phys. Rev. B **32**, 6067.

Sharma, S., D. Kumar, and P. Moskal, 2022, Acta Phys. Pol. A **142**, 428.

Shibuya, K., H. Saito, F. Nishikido, M. Takahashi, and T. T. Yamaya, 2020, Commun. Phys. **3**, 173.

Shibuya, K., H. Saito, H. Tashima, and T. Yamaya, 2022, Phys. Med. Biol. **67**, 025009.

Shinohara, N., N. Suzuki, T. Chang, and T. Hyodo, 2001, Phys. Rev. A **64**, 042702.

Stepanov, P. S., F. A. Selim, S. V. Stepanov, A. V. Bokov, O. V. Ilyukhina, G. Duplatre, and V. M. Byakov, 2020, Phys. Chem. Chem. Phys. **22**, 5123.

Stepanov, S. V., and V. M. Byakov, 2002, J. Chem. Phys. **116**, 6178.

Stepanov, S. V., V. M. Byakov, G. Duplâtre, D. S. Zvezhinskiy, and Y. V. Lomachuk, 2009, Phys. Status Solidi C **6**, 2476.

Stepanov, S. V., V. M. Byakov, and T. Hirade, 2007, Radiat. Phys. Chem. **76**, 90.

Stepanov, S. V., V. M. Byakov, and Y. Kobayashi, 2005, Phys. Rev. B **72**, 054205.

Stepanov, S. V., V. M. Byakova, and P. S. Stepanov, 2021, Phys. Wave Phenom. **29**, 174.

Stinson, R. H., D. King, J. Marsh, J. Fabian, and I. K. MacKenzie, 1980, Phys. Lett. **75A**, 246.

Surko, C. M., M. Leventhal, and A. Passner, 1989, Phys. Rev. Lett. **62**, 901.

Surti, S., A. R. Pantel, and J. S. Karp, 2020, IEEE Trans. Plasma Sci. **4**, 283.

Swartz, H. M., A. B. Flood, P. E. Schaner, H. Halpern, B. B. Williams, B. W. Pogue, B. Gallez, and P. Vaupel, 2020, Physiol. Rep. **8**, e14541.

Tanaka, H. K. M., T. Kurihara, and A. P. Mills, 2006, J. Phys. Condens. Matter **18**, 8581.

Tao, L., R. N. Coffee, D. Jeong, and C. S. Levin, 2021, Phys. Med. Biol. **66**, 045032.

Thirolf, P. G., C. Lang, and K. Parodi, 2015, Acta Phys. Pol. A **127**, 1441.

Toghyani, M., J. Gillam, A. L. McNamara, and Z. Kuncic, 2016, Phys. Med. Biol. **61**, 5803.

Tuomisaari, M., R. H. Howell, and T. McMullen, 1989, Phys. Rev. B **40**, 2060.

Valkealahti, S., and R. M. Nieminen, 1983, Appl. Phys. A **32**, 95.

Valkealahti, S., and R. M. Nieminen, 1984, Appl. Phys. A **35**, 51.

Vallery, R. S., P. W. Zitzewitz, and D. W. Gidley, 2003, Phys. Rev. Lett. **90**, 203402.

Vanderberghe, S., P. Moskal, and J. S. Karp, 2020, EJNMMI Phys. **7**, 35.

Van Dyck, R. S., P. B. Schwinberg, and H. G. Dehmelt, 1987, Phys. Rev. Lett. **59**, 26.

Van House, J., A. Rich, and P. W. Zitzewitz, 1984, Phys. Rev. Lett. **53**, 953.

Van Petegem, S., C. Dauwe, T. Van Hoecke, J. De Baerdemaeker, and D. Segers, 2004, Phys. Rev. B **70**, 115410.

Vaupel, P., A. B. Flood, and H. M. Swartz, 2021, Appl. Magn. Reson. **52**, 451.

Vaupel, P., M. Hockel, and A. Maye, 2007, Antioxid. Redox Signaling **9**, 1221.

Venter, D. J., N. L. Tuzi, S. Kumar, and W. J. Gullick, 1987, Lancet **330**, 69.

Vigo, C., L. Gerchow, B. Radics, M. Raaijmakers, A. Rubbia, and P. Crivelli, 2020, Phys. Rev. Lett. **124**, 101803.

Wada, K., *et al.*, 2012, Eur. Phys. J. D **66**, 37.

Wall, T. E., A. M. Alonso, B. S. Cooper, A. Deller, S. D. Hogan, and D. B. Cassidy, 2015, Phys. Rev. Lett. **114**, 173001.

Wang, C. L., K. Hirata, J. Kawahara, and Y. Kobayashi, 1998, Phys. Rev. B **58**, 14864.

Wang, G., L. Nardo, M. Parikh, Y. G. Abdelhafez, E. Li, B. A. Spencer, J. Qi, T. Jones, S. R. Cherry, and R. D. Badawi, 2022, J. Nucl. Med. **63**, 1274.

Watts, D. P., J. Bordes, J. R. Brown, A. Cherlin, R. Newton, J. Allison, M. Bashkanov, N. Efthimiou, and N. A. Zachariou, 2021, Nat. Commun. **12**, 2646.

Weber, M. H., A. W. Hunt, J. A. Golovchenko, and K. G. Lynn, 1999, Phys. Rev. Lett. **83**, 4658.

Yamazaki, T., T. Namba, S. Asai, and T. Kobayashi, 2010, Phys. Rev. Lett. **104**, 083401; **120**, 239902(E) (2018).

Yan, M., M. Schwaederle, D. Arguello, S. Z. Millis, Z. Gatalica, and R. Kurzrock, 2015, Cancer Metastasis Rev. **34**, 157.

Zabaglo, L., *et al.*, 2013, Ann. Oncol. **24**, 2761.

Zare, M., B. Ghasemi, O. Kakuee, and A. Biganeh, 2022, Radiat. Phys. Eng. **3**, 1.

Zgardzinska, B., G. Cholubek, B. Jarosz, K. Wysoglad, M. Gorgol, M. Gozdziuk, M. Cholubek, and B. Jasinska, 2020, Sci. Rep. **10**, 11890.

Zhang, X., *et al.*, 2020, J. Nucl. Med. **61**, 285.

Zhou, Y., W. Mao, Q. Li, J. Wang, and C. He, 2015, Chem. Phys. **459**, 81.

Zhu, Z., C. W. Harrison, and C.-M. Kao, 2022, arXiv:2206.06463v1.